Master's Thesis 2023

Optical Communication using Nanowires and Molecular Memory Systems

Thomas Kjellberg Jensen

Division of Synchrotron Radiation Research
Department of Physics
LTH | Lund University

Master's Thesis:
Engineering Nanoscience

Optical Communication using Nanowires and Molecular Memory Systems

Thomas Kjellberg Jensen
th6485kj-s@student.lu.se

January 09, 2024

LUND
UNIVERSITY

Master's Thesis work carried out at the Division of Synchrotron Radiation Research,
Department of Physics, Lund University

Supervisor: **Anders Mikkelsen**, anders.mikkelsen@sljus.lu.se
Examiner: **Carina Fasth**, carina.fasth@ftf.lth.se

Abstract

Neuromorphic computational networks, inspired by biological neural networks, provide a possible way of lowering computational energy cost, while at the same time allowing for much more sophisticated devices capable of real-time inferences and learning [1]. Since simulating artificial neural networks on conventional computers is particularly inefficient, the development of neuromorphic devices is strongly motivated as the reliance on AI-models increases. A neuromorphic device inspired by the insect brain and capable of navigation, has previously been proposed, where optically communicating semiconductor nanowires form the basis of the network, and a state-of-the-art molecular dye exhibiting reversible bleaching provides the synaptic weights. This Thesis explores integral sub-components of that device, contributing concrete results towards its realization.

The molecular dye is combined with a nanowire array solar cell device in order to fashion a high-sensitivity nanoscale device with integrated memory functionality. Compared to purely electronic "memory-resistors", this approach features a greater potential for multiplexing due to the wavelength sensitivity of different molecular dye species. The effects of dye concentration, deposition method, film thickness and annealing on the molecular photophysics are explored, identifying starting points for a design optimization process. A high degree of repeatability of the memory functionality is shown, even at prolonged high-intensity illumination.

Additionally, opto-electronic single nanowire ciruits, where the open-circuit voltage generated by the illumination of a *p-i-n* InP nanowire gates an InAs nanowire, are characterized in high-precision Optical Beam Induced Current experiments. Depending on the orientation of the InP nanowire, increase or decrease of the InAs conductance is achieved, suggesting that the circuits could be implemented as excitatory and inhibitory nodes in a nanowire-based neural network. Finally, the optical emission of single InP nanowire devices, previously shown to be able to communicate with each other, is experimentally confirmed and studied.

Acknowledgments

First and foremost, I would like to thank Anders for receiving me so warmly when I first approached you, curious about the InsectNeuroNano project back in 2022, and for always taking your time to meet, discuss and offer feedback over the course of this Master's thesis project. I do not believe I could have been introduced to and guided through the sprawling world of international, multidisciplinary research in any better way.

Secondly I would like to thank all of the PhD's and postdocs whom I have had the privilege of working side by side with during this project, including, but not limited to, Nelia, Vidar, Abhijit, David and Joachim. Additionally, I am very grateful for all of the input and opinions offered by Magnus Borgström, Bo Laursen, Jesper Nygård and Barbara Webb throughout this year.

When finishing my Bachelor's project, I made sure to thank the coffee machine of the relevant Division, and why change a good habit? This time I would like to extend my gratitude to the Solid State Physics coffee machine, for providing many a welcome refreshment between measurements in Asterix and wire bonding.

Populärvetenskaplig sammanfattning

Det är en varm och solig dag. Du ligger på rygg på en grönskande äng och ur ögonvrån ser du ett bi surra av och an tätt ovanför marken, på jakt efter nektar och pollen. Biet tar ett varv runt ängen medan du ligger kvar och funderar ett slag över hur ett sådant bi, som måste flyga hit och dit för att leta upp blommande växter, förmår att hitta hem igen. Dina tankar avbryts av ett surrande: biet närmar sig igen. Men den här gången flyger det målmedvetet fram över ängen, inte längre dansande fram utan i en nästan rät linje rakt ovanför ditt huvud.

Om du hade gissat att biet nu var på väg hem till sin kupa, så hade du gissat rätt. Det är nämligen så att bolevande insekter så som bin, humlor och myror klarar av att ta sig raka vägen hem, oavsett hur krokig vägen under deras utfärd varit. På något sätt måste de hela tiden kunna hålla koll på åt vilket håll "hem" är. Svaret på frågan om hur ett bi förmår hitta hem är komplicerat, men forskare i Lund har lyckats kartlägga delar av humlors hjärna, och där identifierat det nätverk av nervceller som tros ansvara för just denna typ av navigation.

Forskningen som presenteras i denna uppsats syftar till att praktiskt undersöka om man skulle kunna bygga en kopia av detta särskilda nätverk med hjälp av byggstenar som inte är lika fullt komplicerade som de nervceller som utgör insekthjärnan. En av dessa byggstenar är så kallade nanotrådar: en typ av små pinnar mycket tunnare än ett hårstrå. Dessa "nanopinnar" kan fungera både som solceller och LED-lampor. Om man är klyftig kan man placera ut dem på ett sådant vis att varje enskild nanotråd känner av ljuset som de andra skickar ut, i större eller mindre utsträckning. Detta liknar på ett sätt kommunikationen som sker mellan nervceller i en hjärna. Men insekthjärnan, precis som vår egen hjärna, har ett viktigt knep till sitt förfogande: det är nämligen så att kopplingarna mellan nervceller som ofta pratar med varandra stärks, och tvärtom. På det viset kan biet komma ihåg varåt hemmet ligger. I denna uppsats spelas denna viktiga roll av ett färgämne bestående av molekyler som har en lustig egenskap: om man belyser dem, så förlorar de sin färg, men om man sedan låter dem vara i mörker en stund, så återfår de långsamt sin färg igen.

I min forskning har jag undersökt hur ett sådant färgämne beter sig om man bäddar in det i ett tunt lager plast, och vad som händer om man under detta lager placerar en liten solcell bestående av nanotrådar. Lyckosamt nog så beter sig färgämnet mer eller mindre som önskat: i takt med att det bleks, når mer av ljuset solcellen som då genererar en större ström. Om ljuset stängs av för en stund, återfår färgämnet långsamt sin färg, så när ljuset slås på igen dröjer det en stund innan färgämnet åter blekts tillräckligt för att man ska kunna få ut en lika stor ström som innan. Denna självreglerande balansgång mellan ljus och blekning, mörker och färg, verkar alltså kunna bete sig på samma sätt som kopplingar mellan neuroner gör.

Dessutom har jag undersökt om två nanotrådar kan kopplas ihop på ett sådant sätt att belysning av den ena, hindrar elektricitet från att färdas genom den andra. Ytterligare ett annat spår har varit att försöka avgöra hur mycket ljus som en enda nanotråd egentligen kan skicka ut. Sammanfattningsvis kan man säga att resultaten jag kommit fram till bådar gott för en framtida människoskapad minidator som förmår att tänka som ett bi.

Detta kan tyckas avlägset från surrande bin och grönskande ängar, men faktum är att mer och mer av vår energi förbrukas av just datorer, där till exempel det snabbt växande användandet av AI-modeller är en starkt bidragande faktor. Intressant nog visar det sig att hjärn-härmande datorer lämpar sig ypperligt för att utföra den typen av beräkningar som just AI bygger på. Genom att utveckla denna typ av prototyper kan vi alltså bidra till att kraftigt skära ned på kostnaderna i såväl energi som råvaror för just den typen av beräkningar som, vad det verkar, kommer att få en allt större roll i samhället framöver.

Contents

1 Introduction

The rapid increase in silicon-based computational power over the last few decades have brought many new opportunities in technological development and scientific advancements, but at the cost of a sizable increase in energy consumption. Coupled with the ongoing climate change, driven by carbon-emissions from various human activities, this presents a dilemma, with the increased use of computational resources being at odds with a sustainable society. One limiting factor is the von Neumann architecture typically employed in silicon-based computers, in which the CPU and the memory are compartmentalized separately [2]. In light of this, there is a strong motivation to develop new, non-CMOS-based systems which might combine high computational power with low energy consumption. One such field is that of neuromorphic computing, wherein computational systems in greater or lesser extent inspired by the workings of biological neural networks are explored [1][3][4][5].

A quickly growing area of technology (among many) is the integration of small sensors in various objects, allowing for greater control and usability. Similarly, flying drones is another field in which integrated sensors play a huge role. The sensory data can then be used to make various decisions, and typically the data is sent by internet to some external computational environment, which analyzes and makes a decision based on the data, before sending the instructions back to the device. Alternatively, the decision making can be integrated into the device, but oftentimes at the cost of increased energy consumption and device weight. For the case of the drone, this means larger batteries and larger motors, which again increases the energy consumption of the device. For example, the state-of-the-art NVIDIA AI-chip TX2 clocks in at 85 gram and 7.5 Watt [6]. When considering that the human brain, with its much larger complexity and capabilities, consumes about 20 Watt only, it is clear that there is much room for improvement. If the drone additionally should be able to navigate autonomously, an integrated GPS chip is typically required, and so on. Hence, an energy efficient, low-weight integrated computational component fulfilling relevant tasks, would have great applicability in for example autonomous robotics.

Could the field of neuromorphic computing possibly provide solutions to the autonomous navigation issue? It turns out it can. Instead of looking to the human brain for inspiration, the modular and relatively small brains of insects could be used as a template. Owing to the limited resources available and the relative expendability of a single member, colony-based insects tend to have evolved towards minimalistic, highly specified brains, where energy efficiency and "good enough"-robustness is prioritized over plasticity and adaptability. Researchers at Lund University studying the brains of insects such as ants and bumblebees [7] [8], have been able to identify a specific neural network seemingly capable of path integration, residing in the "Central Complex" (CX); a subsection of the insect brain which is preserved across many different species. Navigation is a key issue especially for hive-living insects, as they must be able to return home after a foraging excursion. The path integrating network in the CX performs this task by keeping track of how the insect's velocity changes over time, based on navigational cues such as the sunlight polarization. Summed up, these changes provide the insect with a "home vector" representing the direction of and linear distance to the hive.

It is possible to describe the identified insect neural network as a number of different neurons connected to one another in a specific way. Indeed, any neural network can be decomposed into a number of neurons $\{N_i\}$ which are interconnected by weighted

communication channels $\{w_{ij}\}$. For an input signal S, the transmitted signal strength from $N_i \rightarrow N_j$ is then $S * w_{ij}$. The weights are modified by transmitting a signal; each signal transmitted through a given channel increases the weight of that channel *via* some more or less complicated function $f(S)$. Consequently, channels which are often used, will transmit signals much more easily. It is prudent to also allow for a diminishing of w_{ij} over time; channels which have fallen out of use will suffer a decay back to some minimum coupling strength. The rate k of this decay, and the function $f(S)$, are important parameters for describing a neural network. Figure 1 shows a small neural network consisting of three neurons.

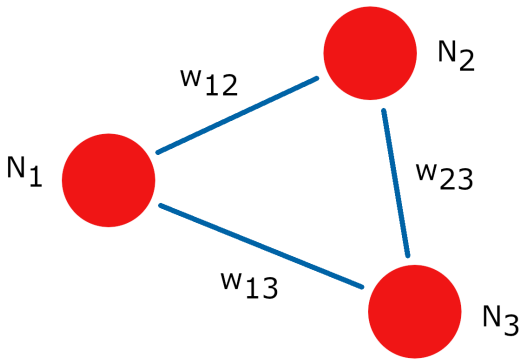

Figure 1: Example of a simple neural network: 3 neurons (N_i) with signal transfer weights w_{ij}.

The abstraction of a biological neural network into the sets $\{N_i\}$ and $\{w_{ij}\}$, implicates the possibility of instantiating an isomorphic neural network using another, possibly abiological substance. The EU-project InsectNeuroNano (part of the Horizon Europe Programme) endeavors to use a combination of optoelectronic nanoscale semiconductor devices and organic dyes exhibiting reversible bleaching to construct a device which realizes the path integrating neural network of the insect CX [9]. Referring back to Figure 1, the semiconductor devices are to embody the neurons, their emission of light the signal, and the transmittance of the dyes the communication channel weight. This design idea is illustrated in Figure 2.

The specific nanoscale semiconductor components chosen for the InsectNeuroNano project are the so-called nanowires (see the SEM image insets in Figure 2). At Lund University, the competence in producing ("growing") these nanometer-thin rods consisting of semiconductor material is very high, making nanowires (NWs) an obvious choice for this project. A big advantage is that the rod-like shape allows for the combination of elements with large differences in lattice constant, since the quasi-1D shape of the NW allows for much greater strain relaxation than a 3D bulk sample. Hence, it is possible to grow group III-V compound semiconductors (such as GaAs, InAs, InP etc.) in the shape of NWs, and this is a major motivation for research and development of NW growth methods. For example, the large number of different III-V material combinations available, allows for a delicate tailoring of the optoelectronic properties of said NWs. Nanoscale components furthermore benefit from having an enhanced absorption cross-section, as a consequence of the light-scattering properties of sub-wavelength structures, even allowing absorption cross-sections larger than the physical size of the structure [12].

The intended organic dyes are of a special class which upon illumination undergo a chemical reaction rendering them colorless, i.e. no longer able to absorb light. But this bleaching is in fact reversible: if left in darkness, the molecules will regain their original

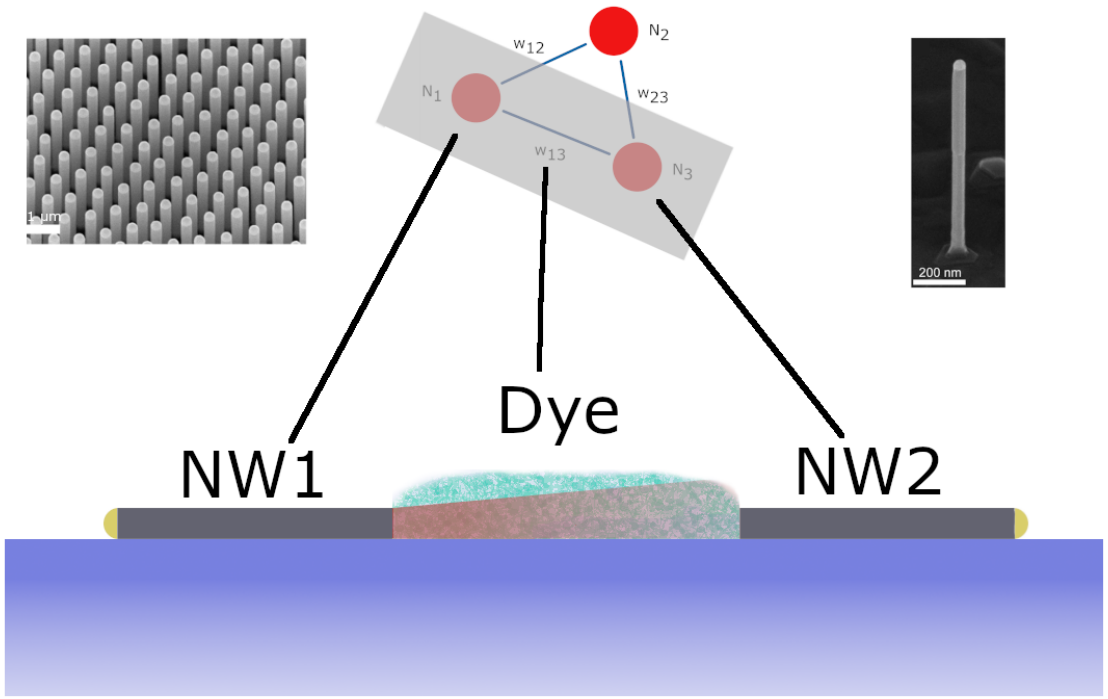

Figure 2: Illustration of the basic idea for realizing a neural network with semiconductor nanowire devices and organic dyes exhibiting reversible bleaching. Each nanowire (NW1, NW2) corresponds to a neuron, the signal is the optical effect emitted by (e.g.) Nanowire 1, and the dye transmittance plays the role of the corresponding weight w. The SEM image to the left shows a section of an array of nanowires, and the SEM image to the right shows a single nanowire. The SEM images are adapted from [10] and [11], respectively.

color over time, with some characteristic rate k. Now one starts to see the similarities with the generalized neural network of Figure 1. If NW1 in Figure 2 is electronically excited, it will emit light. As depicted in the Figure, this light has to pass through the dye layer to reach NW2. Depending on the bleaching state of this dye layer, more or less light will be transmitted to NW2, reflecting whether that same channel has been used more or less. A higher transmitted optical effect will generate a larger current in NW2, fulfilling the weighted signal transfer. More specifically, the photocurrent response of a NW, as a function of absorbed optical effect, follows a sigmoid curve, a behavior which is in fact shared with biological neurons [13] [9].

A simulation based pilot study of the full device showed that an implementation of the CX path integrating network following the design outlined above, using available state-of-the-art technology, would be able to perform the desired navigational task, even allowing for up to 20% noise [9]. In short, InsectNeuroNano shows promise, on the long-term, of delivering a spatially and energetically efficient novel neuromorphic computational device performing a commercially and industrially relevant task.

Neuromorphic computational networks using photonic devices have been suggested and explored previously [14][15][16], but these have required comparatively large, macroscopic optical components, leading to both the circuit size and energy consumption growing rapidly with the number of artificial neurons [17][18]. By instead basing the neuromorphic network on nanoscale components, a substantial reduction of both energy and space requirements can in principle achieved.

However, going to the nanoscale does introduce new types of challenges, mainly related to the handling and accurate placement of single NWs on a substrate, and the appropriate connection of single NWs with each other. Luckily, methods accomplishing such things have already been developed (e.g. micromanipulators and Electron Beam Lithographpy), but the fact remains that a single NW is far more susceptible to external disturbances than, say, a bulk Si transistor. This means for example that what we would experience as a small discharge of static electricity, could ruin an entire circuit of interconnected single NW devices. Another challenge is the small magnitude of the currents involved in the driving of a single NW, and correspondingly, the low optical power emitted from a single NW. Due to for example thermal noise, the signal-to-noise ratio of a NW detecting the light emitted from another NW, could be rather poor, which would limit the possibility to discriminate between different signal intensities. Yet another challenge is the greater relative influence of various material defects on the performance of single NWs, where different surface passivization techniques could be utilized to mitigate such effects.

The production of single NW electronics entails (1) growing an array of a large number (typically 1 million) of vertical NWs, (2) the breaking off of a smaller number of NWs from the growth substrate and the subsequent horizontal placement of these on the sample substrate, and (3) the manufacturing of conducting contacts between the placed NWs *via* some surface deposition technique. In other words, there are quite a few practical steps involved, and it is not immediately obvious that the NWs of the final, processed device, still work as they did when they were freshly grown in array form.

1.1 Lines of Investigations

This work focuses on three distinct lines of investigation related to the overarching, long-term goal of the InsectNeuroNano project: molecular memory systems, NW opto-elecronics, and NW-to-NW optical communication.

1.1.1 Molecular Memory Systems

This line of investigation explores the feasibility and functionality of a combined dye and NW system, where the dye imparts a memory functionality through a reversible bleaching mechanism. The dye was provided by Abbey Meprathu Philip and Bo W. Laursen of the University of Copenhagen, and the NW array (NWA) solar cells used were provided by David Alcer and Magnus T. Borgström of Lund University[10][19].

The work presented here focuses on testing and evaluating different modes of dye deposition in terms of resulting dye layer thickness and molecular kinetics, and evaluating the combined dye+NWA functionality by time resolved illumination measurements at varying intensities.

Referring to Figure 2, these investigations correspond to replacing NW1 with a macroscopic light source, and using a NWA in place of NW2.

1.1.2 NW Opto-Electronics

This line of investigation focuses on optoelectronic evaluation of devices consisting of interconnected single NWs, in which the open-circuit voltage created by illumination of an InP *n-i-p* NW, is used to control the current through an intrinsic InAs NW, *via* a field effect gate. Devices in which the *n*/*p*-segment is connected to the InAs gate will

be referred to as n/p-gated. Optical Beam Induced Current [20] (OBIC) raster scans are used to distinguish between and characterize effects originating from the InP and the InAs NWs.

The InP NWs were produced at Lund University by Abhijit Das and Vidar Flodgren, and the InAs NWs were grown by Joachim Sestoft and Jesper Nygård at the University of Copenhagen, who also assembled the actual devices.

The work presented in this section can be seen as a situation where the current through NW1, and hence the optical effect emitted, is gated by the optical absorption of another NW. Figure 3 shows a hypothetical NW circuit in which n- and p-gating InP NWs control the driving current through a light-emitting InP NW through the gating of an InAs NW. The light emitted by the InP NW passes through a photoreactive dye layer before it absorbed by another InP NW, generating an open-circuit voltage which gates another InAs NW. If for example the left-most p-gating NW is illuminated, it will generate a positive V_{oc} which will increase the current through the InAs NW and hence through the connected light-emitting InP NW as well. The higher current means that the NW will emit more light, and hence that more light will reach the illuminated p-gating InP NW after passing through the attenuating dye layer. This illumination will in turn generate an open-circuit voltage in the illuminated NW, and so on.

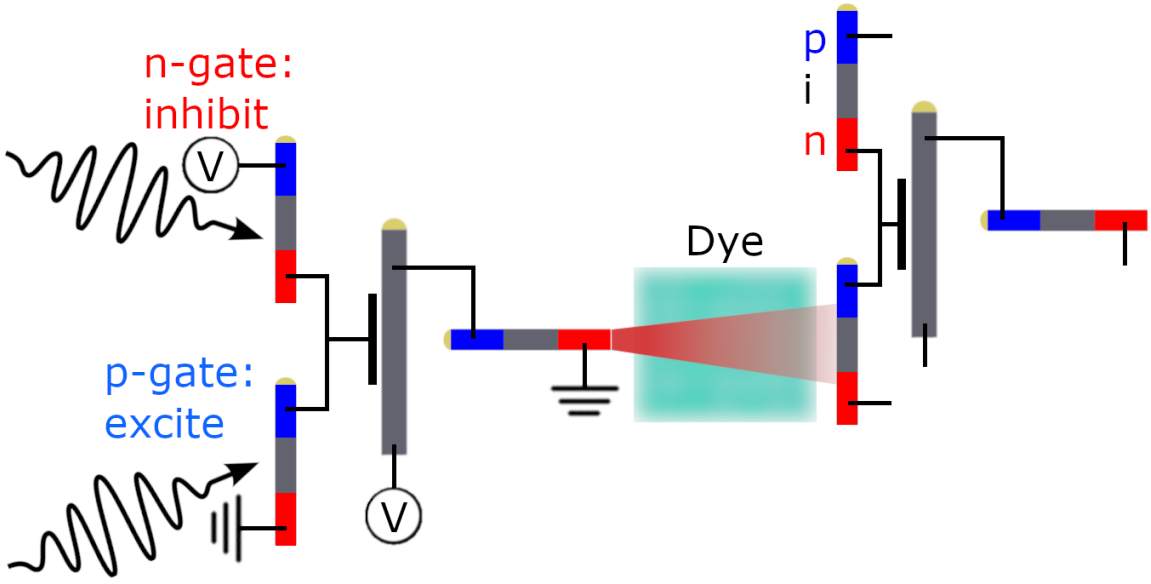

Figure 3: Simple schematic of an NW circuit combining elements studied in Sections 4.1, 4.2, and 4.3. The long NWs are InAs, and the short InP. Red segments denote InP n-doping, and blue segments p-doping.

1.1.3 NW-to-NW Optical Communication

This line of investigation is an auxiliary study of devices where two InP NWs have been aligned so as to facilitate optical communication from one to another. Here, the vertical emission from the individual NWs in one such device, where NW-NW communication was previously confirmed, is studied. This investigation is motivated as an attempt to confirm that optical emission is actually taking place from the NWs in the studied device, which would strengthen the claim that the communication observed was optically mediated.

Optical communication between single NWs is essential for the type of circuit depicted in Figure 3, and those described in Refs. [9] and [13].

2 Theory

In this Section we will introduce a variety of concepts necessary for the understanding of the results presented in this work. NWs made from the direct band gap III-V semiconductors InP ($E_g = 1.34$ eV, $\lambda_g \simeq 923$ nm) and InAs ($E_g = 0.354$ eV, $\lambda_g \simeq 3500$ nm) are studied in various applications in this Thesis, motivating the introduction of relevant solid state physics concepts. The second major area relevant for this work is the field of molecular spectroscopy, motivated by the use of a molecular dye studied in conjunction with NW devices.

2.1 Solid State Physics

In a solid state material, the discrete atomic energy levels overlap, creating continuous "bands" of allowed electron energies. The band structure of any given material is complex, and one often simplifies the description by focusing on the band structure at the point close to zero electron momentum. At this point, the relevant energy bands are often well-described by parabolic functions; using this approximation, the behavior of charge carriers can be modeled semi-classically, by simply replacing the electron mass with the appropriate "effective" mass m^* of the charge carrier in the crystal structure in question. This effective mass is directly related to the curvature of the energy band.

Based on the band diagram, a material can usually be placed in one of three categories: metal, semiconductor, or insulator. For a metal (Figure 4(a)), the highest energy band containing charge carriers is not filled, meaning that only a minimum of energy is required to excite charge carriers into states in which many momentum positions are free, i.e. such that the material can conduct electricity. As a consequence, all photon energies are readily absorbed by such a material, explaining why metals in general are opaque.

For semiconductors and insulators (Figure 4(b) and (c) respectively), the highest energy occupied band is completely filled (the valence band; VB), meaning that an excitation energy larger than or equal to the band gap energy E_g is needed to promote a charge carrier to the next band (the conduction band; CB), i.e. to a state in "open" momentum space. An insulator has a very large band gap energy, while a semiconductor has an "intermediate" E_g, approximately corresponding to optical wavelengths.

A single electron excited across the band gap into the CB, leaves behind a single unoccupied state in the VB. It can be shown that the absence of an electron in this VB sea of electrons, behaves as a charge carrier in and of itself, constituting a quasi-particle termed a "hole". A hole carries a positive charge and, since it occupies the VB, has different effective mass than electrons in the CB. In short, a hole is to the valence band, what an electron is to the conduction band.

Small amounts of impurities can be added to a semiconductor material in order to change its optoelectronic properties. An impurity is any atomic species not being part of the bulk semiconductor material, and a dopant is an impurity which adds additional charge carriers to the semiconductor. Dopants which readily bind VB electrons, hence creating extra holes, are called p-dopants, while a dopant which readily donates electrons to the CB, is termed an n-dopant. Whether a certain atomic species is a p- or n-dopant,

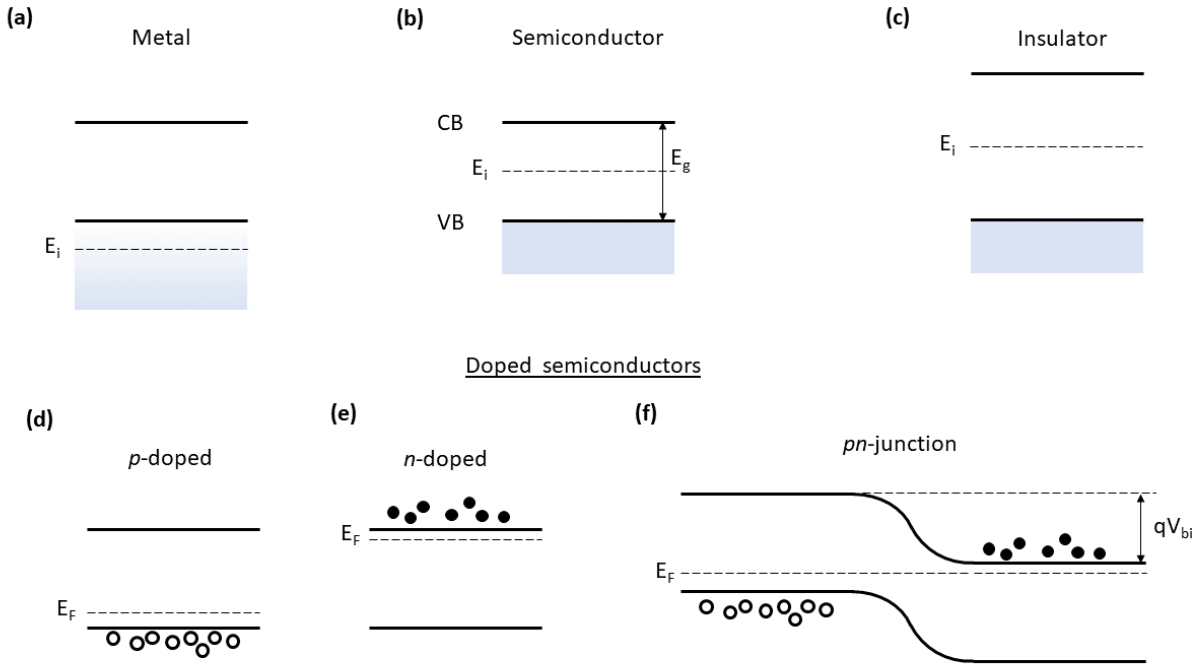

Figure 4: Band diagrams illustrating basic concepts in solid state physics.

thus depends on the atomic valence electron binding energy relative to the VB and CB energies of the semiconducting material. An "undoped" semiconductor is referred to as being "intrinsic".

2.1.1 *pn*-junction

Figure 4(d) and (e) show band diagram schematics of a p-doped and n-doped semiconductor, respectively (open circles represent holes and black dots electrons). Figure 4(f) shows a junction between a p-doped and an n-doped region. At equilibrium, the Fermi energy E_f is constant throughout the pn-junction (or diode), leading to a bending of the energy bands equal to the difference in energy between the two Fermi levels. This difference in energy can be described as the built-in voltage V_{bi} across the junction. Expressed differently, there will be an electric field $\vec{\mathcal{E}}$ spanning the pn-junction.

A pn-junction can be reverse or forward biased by the application of an external voltage V (see Figure 5). In reverse bias, the band bending is enhanced, meaning that close to zero current will flow across the junction. However, any charge carriers generated in the junction region by e.g. photon absorption will be separated and swept away by the $\vec{\mathcal{E}}$ field, giving rise to a measurable current. This is the basis of a photodiode. In forward bias, on the other hand, the band bending is reduced, "opening" the diode and promoting current flow. When both electrons and holes occupy the junction region, there is a non-zero probability of radiative recombination, i.e. photon emission. This is the basis of both LEDs and laser diodes. Notably, any photon energies $E_\gamma \geq E_g$ can be absorbed by a semiconductor, but any photons emitted through recombination will have energies at, or very slightly above, $E_\gamma = E_g$.

The Shockley equation is typically used to model the behavior of a diode:

$$I_D = I_0 \left(e^{\frac{qV}{nk_BT}} - 1 \right) - I_L \tag{1}$$

where I_D is the current through the diode, V the applied bias, q the electron charge, k_B Boltzmann's constant, T the temperature, I_L the current contribution from photogenerated charge carriers, and I_0 the current at large negative bias (reverse bias). n is the ideality factor, describing how well the diode follows the ideal exponential trend of Eq. 1 (where $n = 1$ is the "ideal"). The exponential behavior in Eq. 1 is fundamentally a consequence of the probability distribution Eq. **??**, and indicates that the diode current should increase exponentially with increasing forward bias. An example of this "diodic" behavior is shown in the Figure 6 IV-curve.

A *p-i-n* junction is simply a *pn*-junction where an intrinsic segment is left in-between the *p*- and *n*-segments. This allows for a larger region where photoabsorption leads to viable charge separation and hence a more sensitive photodiode. Additionally, *p-i-n* junctions allow for high doping levels, since any voltage across the junction drops over a longer distance, lowering the maximum $\vec{\mathcal{E}}$ strength, and thus increasing the maximum voltage which can be applied before junction breakdown occurs.

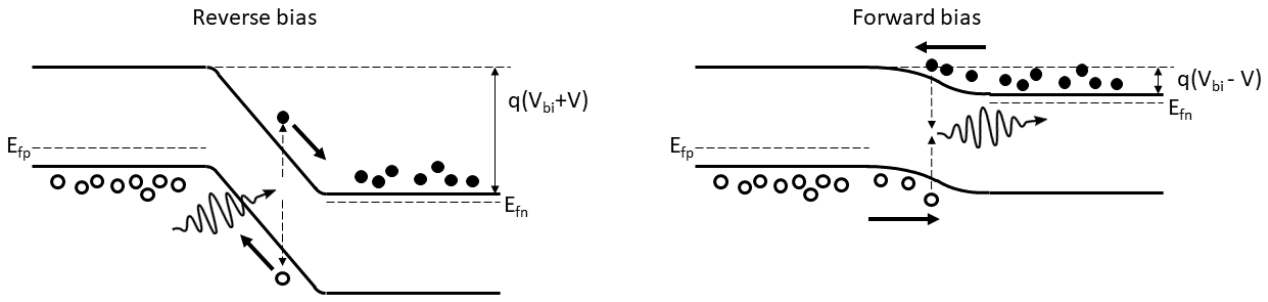

Figure 5: Band diagrams illustrating a diode under reverse (left) and forward (right) bias, as well as the typical optoelectronic applications of each case. The current generated by illumination corresponds to the I_L term in Eq. 1.

Two important concepts in the application of semiconductors as photovoltaic devices are the short-circuit current I_{sc} and the open-circuit voltage V_{oc}. I_{sc} is the current generated by illumination at zero-bias conditions, i.e. the difference between red and black curves at 0 V in Figure 6. In the following, the term "photocurrent" will be used interchangeably with I_{sc}. The V_{oc} is the voltage caused by the build-up of a charge imbalance in the device as a consequence photogenerated charge carriers which occurs when the device is illuminated but its terminals are not connected to each other (zero current).

2.1.2 Field-Effect Transistor

Another common application of semiconducting materials is the field-effect transistor (FET). A Metal-Oxide-Semiconductor FET (MOSFET) is based on a layered structure consisting of a semiconductor substrate on top of which first an insulating oxide layer and then a metallic layer (the "gate") is stacked. When a voltage V_G is applied to the gate, part of the voltage will drop over the oxide layer, and part will induce band bending at the oxide-semiconductor interface. If this band bending is large enough, the electronic properties of the semiconductor can be changed from *n*-type to *p*-type (or *vice-versa*).

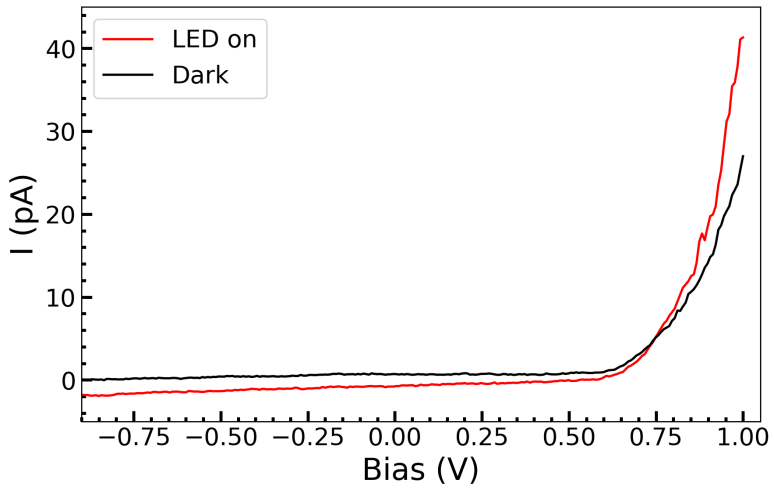

Figure 6: IV-curve of a single InP NW *p-i-n* device, showcasing a typical IV-curve of a diode (black). When the light is turned on (red), the reverse bias current is increased. The difference in current at 0 V bias between the curves, is the short-circuit current I_{sc}. That the maximum forward bias current also is increased under light-on conditions, could be indicative of so-called series-resistances in the device [21].

If the current flow through the semiconductor is dominated by e.g. *n*-type carriers, applying a large, positive V_G will increase the semiconductor conductance. Conversely, a large, negative V_G will restrict the current flow through the semiconductor, decreasing its conductance. Since, again, the band bending depends exponentially on the applied voltage, a field-effect gate allows for a very high degree of control over the current flow in the semiconductor.

In the devices studied in this Thesis, field-effect gates are used to control the current through InAs NWs. Figure 7 shows a cross section schematic of the various layers in this type of FET. The gate voltage is supplied by an InP NW connected to the bottom gate. At the surface of the InAs NW, an electron inversion layer exists, and it is here the majority of the InAs NW conduction occurs. Hence, a negative gate voltage will decrease the InAs conductance, while a positive gate voltage instead would lead to increased conductance. Since NWs by design are very thin, the electric field of the gate will reach through the full NW, giving a homogeneous effect.

2.1.3 Quantum Efficiency

The External Quantum Efficiency (EQE) of a photovoltaic device is defined as the effective number of charge carriers generated per incident photon, giving a measure of the efficiency of the device. "Effective" in this context means the number which can actually be used to generate work, i.e. which exit the device through the device contacts. The Internal Quantum Efficiency (IQE), on the other hand, describes how many charge carriers are generated per photon absorbed by the semiconductor material, a number which often is different from the EQE due to various losses occurring outside of the photoabsorbing region of the device.

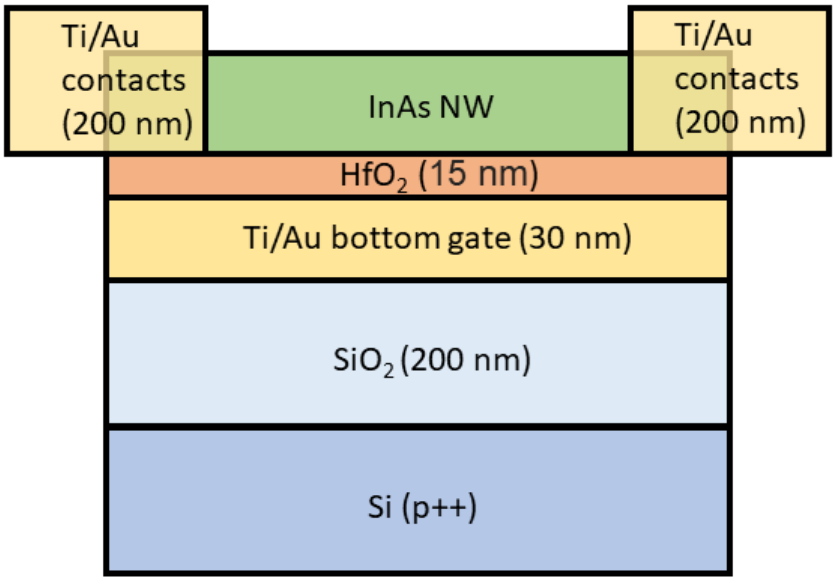

Figure 7: A not-to-scale schematic showing a cross-section of the field-effect gate structure used to gate the InAs NWs in the opto-electronic NW circuits studied in this Thesis. The bottom gate is connected to an InP NW, while the InAs NW current is measured through the contacts.

2.1.4 III-V material NWs

Certain mono-atomic crystals are "natural" semiconductors, namely those belonging to group IV in the periodic table. Of these, silicon (Si) is the most commonly used, being an integral part of all modern conventional computers and electronics. But combinations of other elements will also form a semiconductor material: III-V and II-VI group materials.

Common III-V materials include GaAs, InAs and InP. A common problem in producing devices consisting of combinations (e.g. InAs/InSb) of such compound semiconductors, is the crystal lattice mismatch between the two different materials. If one tries to grow such heterostructures in bulk, the lattice mismatch will contribute two defect formation originating at the interface between the two materials. There are many types of such defects, see for example [22] for a discussion of these. The end result is however a flawed material which does not have the desired properties, making this production method ill-suited for III-V heterostructure semiconductors.

One way of mitigating the defect formation in III-V semiconductors is to not grow them in 3D bulk form, but in quasi-1D structures called nanowires (NWs). NWs have a large aspect ratio, typically being a few micrometers long and between 20-300 nanometers in diameter [11][23]. Additionally, NWs exhibit an absorption cross-section σ at optical wavelengths which is larger than their physical size, meaning that they in a sense will absorb more light than which seems geometrically possible. But this is indeed possible, since the sub-wavelength dimensions of NWs allow them to support Mie scattering modes [24]. For an example of this, please see Ref. [12]. NWs are typically grown in "arrays" consisting of several hundred thousand NWs; Figure 8 shows a SEM image of a section of such an array.

By supplying various dopants during growth, it is possible to manufacture NWs featuring e.g. *pn*- or *p*-*i*-*n* junctions (see above). Interestingly, InAs NWs which are grown nominally undoped, will still acquire an *n*-type character [11].

It is a known phenomenon than InAs NWs can exhibit a negative photoconductivity

response (NPC) [23], manifesting as an exponential decrease in conductance at low illumination intensities. In addition to the NPC, these NWs also show "normal", positive photoconductivity (PPC), which however first becomes noticeable at higher intensities. A model is put forward in Ref. [23], in which the NPC effect is explained by the presence of long-lived surface trap states. At low illumination intensities, electrons are excited into these trap states, lowering the amount of available charge carriers and hence decreasing the NW conductance. Due to the finite number of available trap states, the NPC effect will saturate at high enough intensities. Any further increase of illumination intensity beyond this point, will contribute solely to the creation of new electron-hole pairs, i.e. the NW will show the "normal" PPC response.

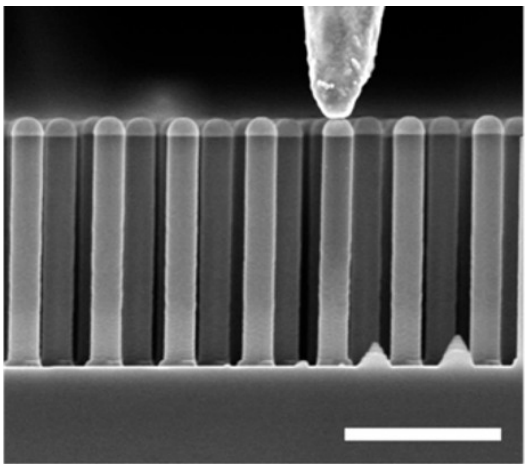

Figure 8: SEM image of an InP NW array, where one NW is contacted by a probe. The scale bar is 1 μm. Figure adapted from [19].

2.2 Molecular Chemistry & Spectroscopy

A molecular dye is any molecule which strongly absorbs light at some characteristic wavelength. The absorbance of light transfers the molecule to an electronically excited state, from which it will decay back to the ground state. Different de-excitation pathways exist, and they can be divided into two main groups: radiative and non-radiative. Radiative de-excitation is any process where the excitation energy is emitted as a photon. Non-radiative pathways include the excitation of vibrational states, as well as more complex rearrangements of the atomic nuclei leading to metastable changes of the molecular conformation.

The Beer-Lambert law [25] describes the attenuation of light passing through a solution in which a photoabsorbing molecule is dissolved:

$$I = I_0 * T = I_0 * 10^{-A} = I_0 * 10^{-\epsilon l c} \tag{2}$$

where I_0 is the input light intensity, T the transmittance of the solution, A its absorbance (or "optical density"), ϵ the molar absorption coefficient of the absorbing molecule, c the molar concentration of the molecule in the solution, l the optical path length, and I is the output light intensity. Typically, ϵ is expressed in units of $\mathrm{M^{-1}{\cdot}cm^{-1}} = \mathrm{L{\cdot}mol^{-1}{\cdot}cm^{-1}}$, l in cm, and c in M [25] (the capital L denotes liters).

It is important to note that while transmittance T is the fraction of light which is transmitted, absorbance A is defined as

$$A = -\log_{10} \frac{I}{I_0} \neq 1 - T \tag{3}$$

A common issue in optical spectroscopy is the so-called photobleaching of the studied molecules. This is a catch-all term which refers to any photo-induced chemical reaction which irreversibly changes the properties of the molecule in a way which renders it transparent to the illumination used. For example, in fluorescence spectroscopy, photobleaching refers to the loss of molecular fluorescence. As a rule, photobleaching is an inevitable result of prolonged illumination [25].

2.2.1 Donor-Acceptor Stenhouse Adduct dyes

In addition to the irreversible photobleaching discussed above, there exists molecules which exhibit *reversible* bleaching, explained by the availability of a metastable state in which the molecule has changed its conformation in a way which affects its optical properties. A subclass of these molecules is the Donor-Acceptor Stenhouse Adduct (DASA) dyes, first synthesized and described by Helmy *et al* in 2014 [26]. The DASA dyes build upon developments and discoveries originating from certain colored salts described by Stenhouse in 1870 [26].

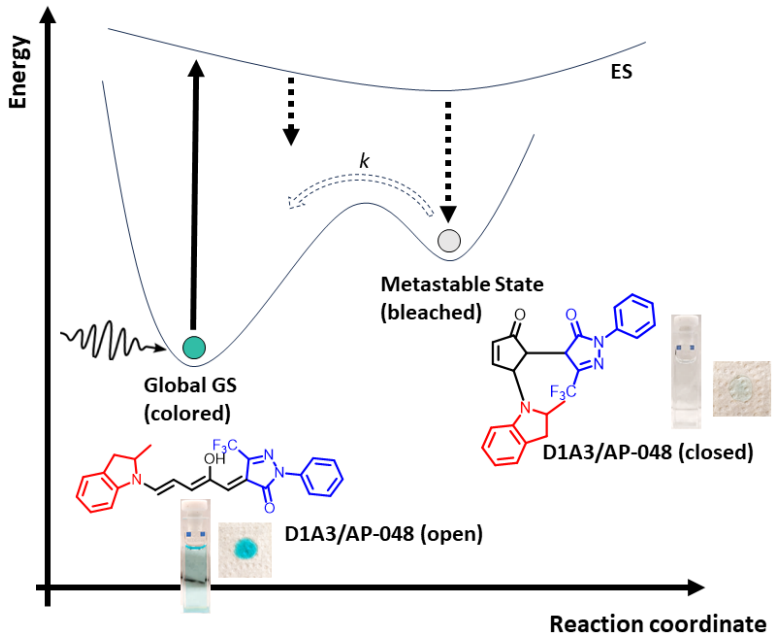

Figure 9: Simplified schematic of molecular potential energy surfaces (PES) explaining the photophysics of DASA dyes. Chemical structures and photographs courtesy of Abbey Meprathu Philip.

In Figure 9, the central concepts of DASA dyes are shown schematically. The y-axis shows the energy of the molecular electronic states here considered, and the x-axis "reaction coordinate" represents the sum of changes in the nuclear coordinates relevant for the reaction considered. The ground state potential energy surface (PES) has two relevant, distinct states: the global ground state (GS), in which the molecule is in its

open, colored conformation, and a metastable state in which the molecule is in its closed, colorless (or bleached) state. Upon photon absorption, the molecule can be promoted from the global GS to the electronically excited state (ES). The molecule will move along the reaction coordinate to the ES PES minimum, from which it will de-excite non-radiatively to the metastable state. From the metastable state, the molecule will decay back to the global GS by thermal excitation, with a reaction rate k (the "back-reaction" rate). Note that de-excitation is principally possible from any point on the ES PES, as indicated by intermediate dashed arrow, meaning that not all excited molecules actually reach the bleached state.

The longevity of the bleached state is in other words determined by the back-reaction rate. The depth of the bleached state local minimum can be tailored by altering the molecular structure, enabling the synthesis of a range of DASA dyes with different k-values, for a given temperature. For a given DASA molecule, k can be increased by increasing the available thermal energy. The absorption spectrum of these dyes can be likewise be tailored; a few examples are given in Figure 10. For clarity, it should be emphasized that both k and the absorption spectrum depend on the chemical structure of the molecule, meaning that one can not be changed independently of the other.

Note that the description given here is simplified; in reality, there exists a large number of different excited states, and the potential energy surfaces exhibit a more complicated topography, including a number of intermediate states, than the smooth curves in Figure 9.

The molecular structures shown in Figure 9 depict the specific DASA dye D1A3/AP-048 which was used extensively in the work presented here (henceforth denoted AP-048). The photographs show the dye color under visible light illumination in liquid and solid form, for the colored and bleached state respectively. The dye was synthesized and provided by Abbey Meprathu Philip and Bo W. Laursen at the University of Copenhagen.

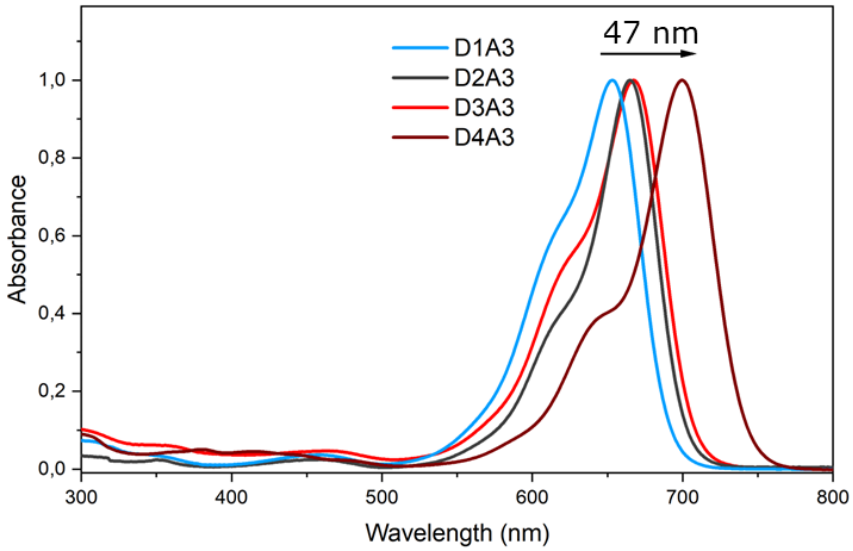

Figure 10: Selection of DASA absorption spectra in toluene, courtesy of Abbey Meprathu Philip. D1A3 (AP-048) is the dye used in this work.

2.2.2 DASA-kinetics Model

To describe the optical properties of a system consisting of a given DASA dye using Eq. 2, we must consider two molecular concentrations: c_{on} and c_{off}, for the absorbing and bleached populations respectively. Assuming that we can neglect the possibility of any other molecular states, we get the total concentration c_{tot} as

$$c_{tot} = c_{on} + c_{off} \tag{4}$$

Eq. 2 can then be rewritten as

$$I = I_0 * T(c_{on}) = I_0 * 10^{-\epsilon l c_{on}} = I_0 * 10^{-\epsilon l \left(c_{tot} - c_{off}\right)} \tag{5}$$

at steady state. To describe the time-dependence of the system, we must take the decay rate of c_{off} into account, as well as the possibility of a time-varying input intensity I_0. Assuming the $I_0(t)$ is known, the time-dependence of the system is determined completely by $c_{off}(t)$.

The bleached molecular population is created by absorption of photons, and destroyed by thermal de-excitation. We assume now that the temperature is constant over time, such that the thermal de-excitation rate k also is constant over time. Assuming that photons are incident at a time-varying rate $I_0(t)$, the fraction of those photons absorbed by molecules in the c_{on} population is, from Eq. 2, $I_0(t) * (1 - T)$. Of the excited state molecules created in this way, only a fraction will form the bleached state (see above). We can call this fraction Φ, the quantum efficiency of bleached state formation. The full c_{off} population creation term C now reads

$$\begin{aligned} \mathsf{C} &= I_0(t) * \Phi * (1 - T) \\ &= I_0(t) * \Phi * \left(1 - 10^{-\epsilon l \left(c_{tot} - c_{off}(t)\right)}\right) \end{aligned} \tag{6}$$

where we have used Eq. 5 and included the explicit time-dependence of c_{off}. Based on the above assumptions, the c_{off} destruction term D is simply

$$\mathsf{D} = -k * c_{off}(t) \tag{7}$$

The net change of c_{off} over time is the sum of C and D, giving the following differential equation:

$$\begin{aligned} \frac{\mathrm{d}c_{off}(t)}{\mathrm{d}t} &= \mathsf{C} + \mathsf{D} \\ &= I_0(t) * \Phi * \left(1 - 10^{-\epsilon l \left(c_{tot} - c_{off}(t)\right)}\right) - k * c_{off}(t) \end{aligned} \tag{8}$$

which can be solved numerically.

The model described here is similar to the treatment given in [27], in which the authors arrive at an expression corresponding to Eq. 8. However, while $k = 0$ is assumed in the majority of investigations in Ref. [27], we here explicitly consider the situation when $k \neq 0$, as anything else would fail to describe a crucial part of the molecular kinetics at hand.

2.3 Memory Theory

The concept of memory employed in this work is extremely simplified. We will consider a "one-channel" memory only, corresponding to the coupling strength between two single neurons.

We will broadly identify two types of memory functionality: a read/write memory, and a "dynamic" memory. A read/write memory corresponds to the memory functionality of e.g. a computer hard drive, and a dynamic memory corresponds to the memory functionality exhibited by neuron communication weights in biological neural networks.

An artificial neural network (ANN) commonly employs a combination of these two generalized memory types. When the ANN is trained, the weights are altered through error back-propagation [28]; but after completed training, the weights are kept constant in order to achieve predictable ANN behavior.

2.3.1 Read/write memory

Here we will employ a "*read*" and "*write*" terminology, specifying two distinct types of input. An ideal *read* input should give an output which accurately reports on the current memory state, without altering the state in question. An ideal *write* input, on the other hand, should change the memory state. Since we are here considering an non-von Neumann integrated memory+processing system, both the *read* and *write* input will be supplied by the same component. Hence, the main dimension along which the two types of input can be distinguished is their intensity, I_{write} and I_{read}. This leads to a situation where $I_{write} > I_{read}$, and where I_{read} is small enough to not alter the memory state significantly, and I_{write} is large enough to change the memory state. Figure 11, illustrates both the *write* (top) and *read* (bottom) processes.

However, there exists a lower bound for I_{read} in that the *read* input must generate an output which is strong enough to be detected by the output detector. Additionally, there exists an upper bound for I_{write} in that the memory must not be saturated before the system has completed its task. If that were to happen, any subsequent *write* input would not affect the memory, and hence be lost to the system. Taken together, these requirements define an optimization space, the shape of which is set by the output detection resolution, the memory reactivity and storage size, the available intensity range of the input signal generator, and the I_{write} integrated over the intended usage time of the system.

2.3.2 Dynamic memory

The concept of a dynamic memory was briefly described in Section 1, in terms of the communication channel weight w_{ij} between two neurons N_i and N_j. Whenever a signal S is transmitted through the channel, w_{ij} is increased *via* some function $f(S)$; when the channel is not used, w_{ij} decays over time at some rate k.

This type of memory is perhaps most easily described as a learning-oriented memory. Such a memory is, in contrast to the read/write memory, not intended for storing abstract, specific data, but instead meant for applications in which a large degree of continuous adaptability is desired. Imagining a large number of interconnected neurons, a signal might take different paths throughout this network. Since the synaptic connections can be weighted differently, certain pathways could more easily transmit signals than others. Likely, some synaptic pathways represent more important processes or actions, meaning

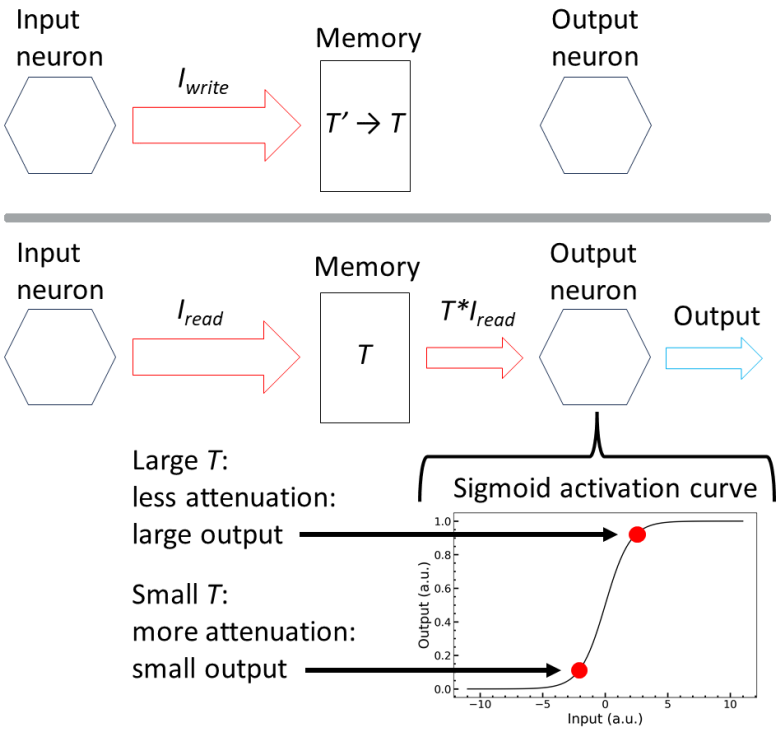

Figure 11: Schematic showing the two principle memory input types considered here: *write* (top) and *read* (bottom).

that any input relevant to those pathways is of vital importance to the system. In this way, it makes sense to increase the sensitivity of those pathways, such that even very low intensity signals will be picked up and carried forward along the synaptic path in question.

In the context of dynamic memory, there is no separation of signals into different categories such as *read* and *write*; the weight-changing function $f(S)$ should be continuous over the signal intensity range. Of course, this does not mean that $f(S)$ must be linear with S; in biological contexts, a logarithmic $f(S)$ is for example not unheard of [7].

3 Methods

3.1 Simulations

To illustrate the working principles of dye-based memory, a script solving Eq. 8 was constructed, using the 8:th order Runge-Kutta method DOP853 [29] as implemented in Python 3.8. In all simulations, a value of the wavelength dependent molar absorption coefficient ϵ corresponding to the absorption peak of the D1A3/AP-048 dye was used (see the D1A3 curve in Figure 10).

3.2 Optical Beam Induced Current

Optical Beam Induced Current (OBIC) is a spatially resolved optoelectronic measurement technique. The OBIC measurements presented in section 4.2, were carried out using a modified Unisoku SPM setup. In these measurements, the STM probe was not used. Figure 13 gives a schematic overview of the optical components used in the measurements, and how they relate to the electronic contacts of the Unisoku setup. The heatmap in Figure 13 shows an example of the results of an OBIC scan, with current as a function of position.

The sample to be studied is mounted on the Unisoku sample holder, which is divided into four separate conducting islands (see Figure 12), allowing for a maximum of four simultaneous wire bonds to the sample. The holder is inserted into the sample stage of the actual setup, where four metal clamps contact each of the four conducting islands of the sample holder.

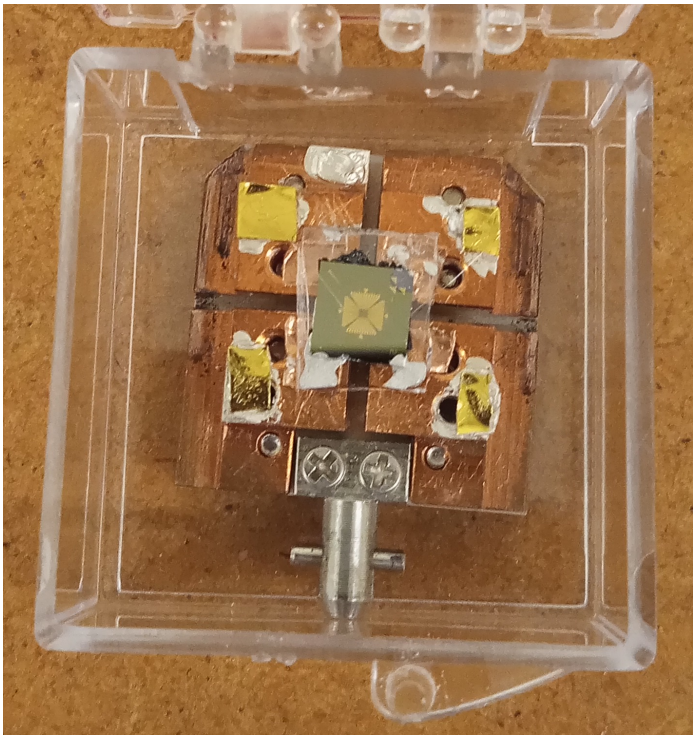

Figure 12: Photograph of a Unisoku sample holder with a sample mounted. Note that the holder is partitioned into four isolated copper "islands".

The objective lens is situated above the sample, and the stage can be moved in x, y

and z by piezoelectric actuators with high precision. By raster scanning the sample with the laser diode beam focused on the sample surface, while simultaneously measuring the current through a device within the scan area, a spatially accurate 2D map of current as a function of beam spot position, can be generated. The spatial resolution is set by the stage movement resolution and the beam spot size. Since the spatial precision of the stage is at sub-Å levels [30], the beam spot size ($\sim$ 1 μm) is the limiting factor of the OBIC resolution.

The optical components, including the objective, are mounted together on a platform which can be mechanically raised and lowered.

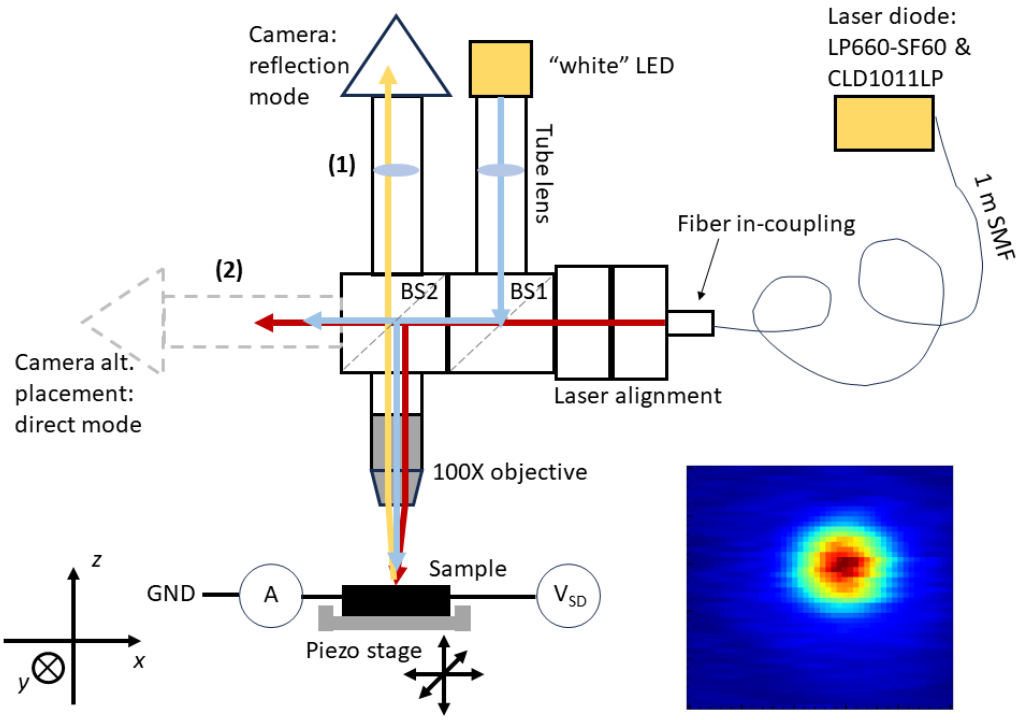

Figure 13: Schematic showing the components used in the OBIC measurements. The LD output is guided through a single-mode optical fiber and then ported into the setup proper through two components which are used to align the LD light with respect to the rest of the setup. The optical components are mounted together and can be raised or lowered in order to focus the objective lens on the sample. The piezo stage on which the sample is mounted allows for movements along all three spatial axes.

3.2.1 Light Sources & Detection

The optical setup utilizes two different light sources, and a monochrome CMOS digital camera (Thorlabs DCC1545M-GL) for optical detection.

A white-light LED (Thorlabs MNWHL4) was used for broad sample illumination, and a LP660-SF60 (Thorlabs) laser diode (LD) with a central wavelength of $\sim$ 660 nm, controlled using a CLD1011-LP laser diode driver (Thorlabs), was used for measurements requiring position-specific illumination. The laser output is ported to the optical setup using a Single Mode Fiber (SMF), and is guided through components which allow for the angular and translational alignment of the LD beam relative to the remaining optical components. The LD beam then passes through two consecutive 50:50 beam split-

ters (Thorlabs CCM1-BS013/M, 400-700 nm), with one part of the beam being directed through the objective lens onto the sample, and one part passing straight through the beam splitters, parallel to the xy-plane, arriving at position (2) in Figure 13. In order to quantify measurements performed with the LD, a calibration curve for the specific setup used was established by measuring the LD optical power at a position corresponding to the "Sample" position in Figure 13. The power measurements were conducted using a Thorlabs S130C Si photodiode sensor, together with the PM100D power meter console. The power of 1.6 nW registered at $I_{LD} = 0$ mA constitutes the unavoidable background illumination mainly originating from the screen of the computer controlling the Unisoku setup and leakage from under the door to the lab room.

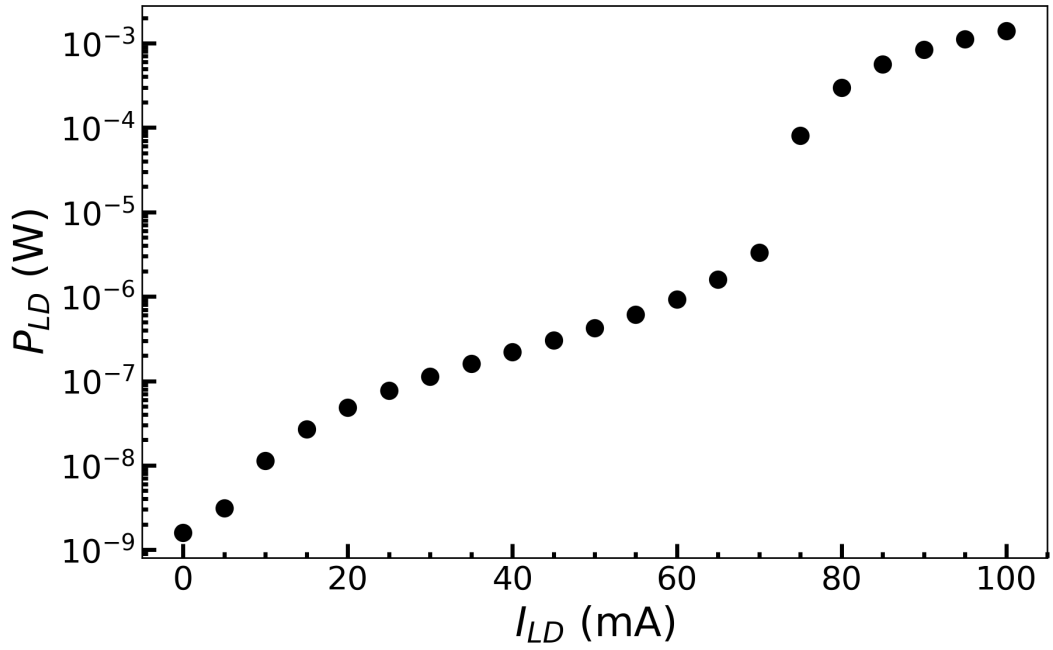

Figure 14: Calibration curve for the LD on a log-lin scale. I_{LD} is the LD driving current and P_{LD} is the LD total optical power incident on the sample in the setup used (see Figure 13 for reference).Note the lasing threshold at $I_{LD} \simeq 75$ mA.

The broad LED light is similarly guided through the beam splitters, with one part illuminating the sample through the objective, and one part impinging on position (2) in Figure 13.

The CMOS camera can be placed in either of two positions: (1) or (2). Position (1), or "reflection mode", allows for imaging of the sample through the objective lens, by detecting the input LED or LD light reflected on the sample, as well as detecting any light emitted from the sample along $\sim z$. Position (2), or "direct mode", allows for direct imaging of the input light, which is useful for characterizing e.g. the beam profile or intensity.

A 100X objective lens (Olympus LMPLFLN100X, NA= 0.8) was used for the majority of experiments, with a 20X objective (Olympus LMPLFLN20X, NA= 0.4) being used to a lesser extent.

3.2.2 Circuitry

Figure 15 shows the circuit diagram for the Unisoku setup as used here. As noted above, the sample holder has four distinct conducting regions from which bond pads on the sample can be connected to by wire bonding. For illustrative purposes, Figure 15 contains an example device connected to the setup: a single NW device is connected to contact A and B, and contact C is connected to a field effect gate acting on the NW. The NW can be biased using voltage source V1 (i.e. V_{SD}), and V2 (V_G) controls the gate voltage. The current through the NW is passed through a Femto DLPCA-200 amplifier (AMP), and measured by ammeter A1. The gray region denotes the sample holder, while the green region denotes the actual sample on which the semiconductor device is placed. The leads straddling the gray region correspond to the wire bonds, and the leads in the green region correspond to the Ti/Au bond pads and leads which have been deposited on the sample.

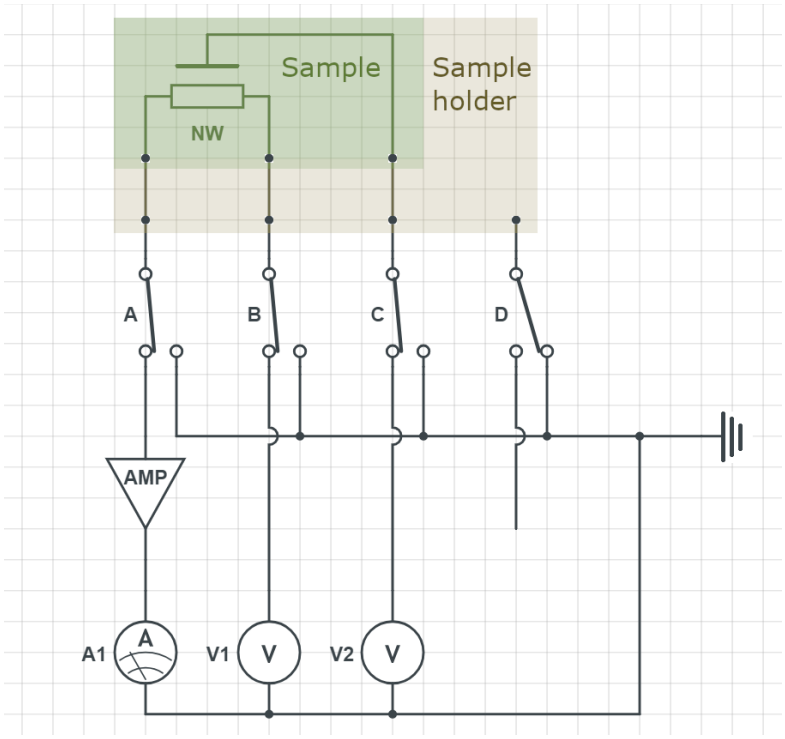

Figure 15: Circuit diagram of the Unisoku setup. The diagram shows an example situation where a single NW is connected to contact A and B, and contact C is connected to a field effect gate acting on the NW. V1 and V2 are voltage sources, and A1 is the Unisoku integrated ammeter. AMP is the external Femto DLPCA-200 amplifier.

3.3 Dye deposition

In order to be able to deposit the DASA dye AP-048 on substrates, the pure dye (in solid form) was dissolved in a 1:9 part solution of toluene:dichloromethane, together with the polymer PAMS: poly(α-methylstyrene). The dye concentration can be described either as the molar concentration in the solvent, the or dye-to-polymer weight percent (%-wt); the former is relevant for the solution, and the latter for the thin film formed after deposition when all solvent has evaporated.

Some of the solutions were prepared by Abbey Philip in Copenhagen and transported to Lund, and some were prepared locally at the Division of Chemical Physics. Over the course of the project, four different concentrations were trialed: 5 mM (1%-wt), 10 mM (2%-wt), 15 mM (3%-wt) and 24 mM (5%-wt).

Two different deposition methods were used: drop casting and spin coating. Drop casting is simply the act of depositing a droplet of the solution on a stationary substrate by pipette. In spin coating, the sample is placed on a "chuck" which holds the sample in place by vacuum suction. The chuck is then rotated at high speeds ($\sim 1000 - 8000$ rpm), while the solution is deposited at the center of the sample surface. The rotational acceleration of the sample will force the deposited solution to spread radially outwards, covering the sample. As the solution spreads, the solvent will evaporate leading the polymer to form a film which clings to the sample. Most of the deposited solution is thrown off of the rotating sample in this way, leaving a homogeneous film on the sample.

The dye was deposited both on transparent sapphire samples and on a NW array (NWA) solar cell device. Dye deposition was carried out in the Lund Nano Lab.

3.4 External Quantum Efficiency characterization

The Bentham PVE300 combines two current-controlled lamps with a lock-in amplifier in order to provide spectrally resolved External Quantum Efficiency (EQE) characterization of photovoltaic devices, as well as transmission spectroscopy using an integrating sphere. The Bentham setup was used for transmission measurements on the dye+sapphire samples as well as EQE measurements on the dye+NWA system.

In an EQE measurement, the tested device is illuminated by a monochromatic probe, and the photocurrent extracted from the device as a function of wavelength is measured. The optical power of the probe as a function of wavelength is calculated by calibrating the setup using a photodetector of known responsivity (A/W^{-1}). From this, the number of photons incident per second on the device can be derived. Based on this, the EQE of the device can be calculated. EQE is often reported as a percentage, where 100% corresponds to 100% of the incident photons being converted to charge carrier pairs which are successfully extracted from the photovoltaic device.

3.5 Solar Simulator G2V Pico

The Variable Solar Simulator G2V Pico is, as the Bentham setup, designed for the characterization of photovoltaic devices, and features two-probe electric contacting capabilities together with a large number of calibrated LEDs, which are individually controllable. As such, the Solar Simulator can provide a large variety of finely tuned illumination settings, mainly focused on emulating the solar spectral irradiance. In this work, only a single of the available LEDs was used: providing illumination with a central wavelength of ~ 660 nm, and a spectral range of 633-711 nm. This LED was chosen since it was the one which provided the best overlap with the AP-048 absorption spectrum (D1A3 in Figure 10). The Solar Simulator was used both for the bleaching of the dye+sapphire samples and the time-resolved illumination measurements on the dye+NWA system.

In the following, the Solar Simulator illumination intensities will be given in the arbitrary units used by the controlling software. Please refer to Table 5 in Appendix B for a conversion to units of mW/cm^2.

3.6 Conductance

Some of the results presented in Section 4.2 report on the conductance G of InAs NWs in units of Siemens ($S = 1/\Omega$). The conductance was arrived at by doing an IV-sweep from -5 mV to +5 mV of the NW in question and fitting a linear function to the resulting data. The conductance was then taken as the slope of the fit. All relevant IV-curves were linear; a necessary requirement for this approach to work.

For improved comparability, the conductance data will often be presented as a ΔG-value, where $\Delta G = 0$ is defined as the conductance of the first data point of the measurement in question.

4 Results & Discussion

In this Section, the results pertaining to each of the three lines of investigation will be presented in order.

4.1 Molecular Memory Systems

The results presented in this Section pertain to the subsystem highlighted in Figure 16. Section 4.1 starts out with a description of two different simulations and how they relate to the two memory functionalities described above, before giving in-depth presentation of the results from experiments tentatively exploring the uses and limitations of a polymer-suspended DASA dye as a memory system. Two types of samples are studied: those where the dye is deposited on sapphire (Figure 17a), and those where it is deposited on an NWA (Figure 17b).

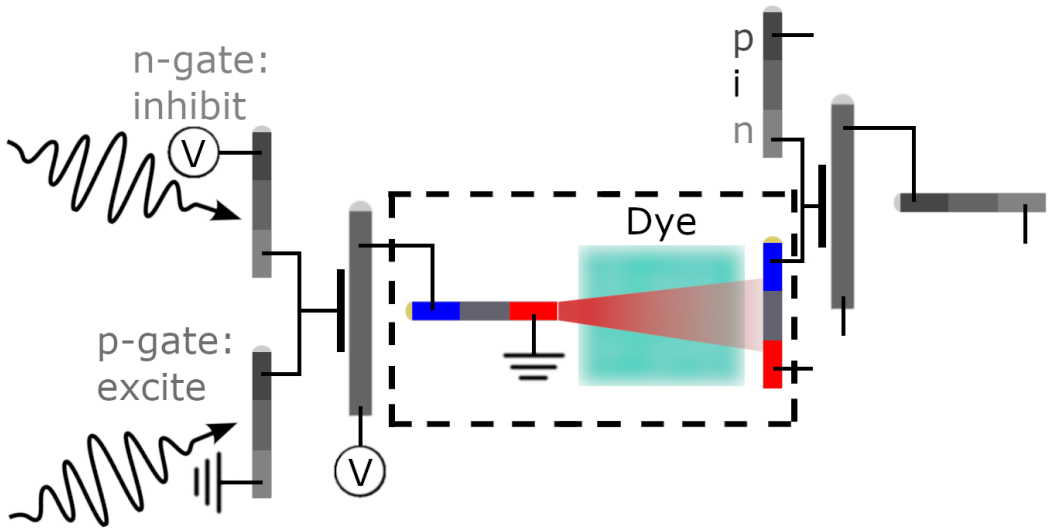

Figure 16: The highlight shows the part of Figure 3 which the results presented in this Section pertain to.

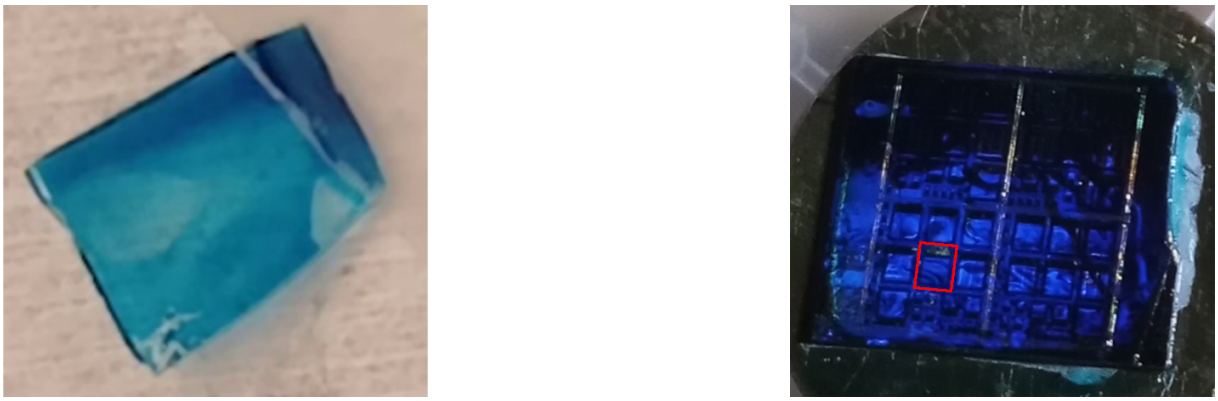

(a) **(b)**

Figure 17: (a) Example of a dye+sapphire sample. (b) Example of a dye+NWA sample. The red box delimits one of the NWAs on the sample.

4.1.1 Simulations

Figure 18 shows the results extracted from a numerical solution of Eq. 8. In Figure 18 top, the normalized input optical intensity (blue) is plotted together with the transmitted intensity (red) on the right hand axis. The bleached state concentration (c_{off}, cyan) is plotted on the left hand axis. The input light is modeled as Gaussian pulses. The four lowest intensity pulses fill the role of *read* input, while the two sets of higher intensity pulses are the *write* pulses. The bottom part of Figure 18 shows the transmittance of the simulated dye layer, and the inset shows the normalized transmitted *read* peak intensities, with the earliest *read* pulse giving the baseline memory value.

As is seen, after a certain number of high intensity pulses, the transmittance saturates at about 0.7. When the pulse intensity is decreased (at $t = 550$ s), the transmittance decays to a lower value at which it again starts to saturate. This illustrates how the memory will continuously adapt to the input intensity. When the *write* input is turned off, the bleached state concentration, and hence the transmittance, decays exponentially back to the initial value. If the half-life of the bleached state is significantly longer than the intended operational time of the memory, this decay will be approximately linear. Successful memory utilization depends on the ability of the detector to discriminate between the different transmitted *read* intensities. A greater absolute difference can be achieved by increasing the input *read* intensity.

Table 1: Simulation parameters used in the solution to Eq. 8 presented in Figure 18.

ϵ	10^5 $\mathrm{M^{-1}cm^{-1}}$
l	$2 \cdot 10^{-4}$ cm
c_{tot}	24 mM
k	$4.33 \cdot 10^{-3}$ $\mathrm{s^{-1}}$
Φ	$5 \cdot 10^{-3}$

Figure 19, on the other hand, illustrates a dynamic type memory. We have now decreased the back-reaction rate k by a factor of 10 (see Table 2), in order to exaggerate the difference from the read/write type memory. The transmittance in Figure 19 starts out at 0.3, but is rapidly raised to 0.95 by intense illumination. At $t = 2000$ s, the intensity has gone down, but the transmittance (i.e. the weight w) remains high. Beyond $t = 3000$ s, the input intensity rapidly falls off again, and in this region we see a steady decline of the transmittance, at a rate which is significantly slower than the decrease of input intensity. The delay in transmittance decrease *vis-a-vis* the input intensity, constitutes the memory effect in this case; the communication channel retains a certain degree of "openness" imprinted by the earlier signal strengths.

Table 2: Simulation parameters used in the solution to Eq. 8 presented in Figure 19.

ϵ	10^5 $\mathrm{M^{-1}cm^{-1}}$
l	$2 \cdot 10^{-4}$ cm
c_{tot}	24 mM
k	$4.33 \cdot 10^{-4}$ $\mathrm{s^{-1}}$
Φ	$5 \cdot 10^{-3}$

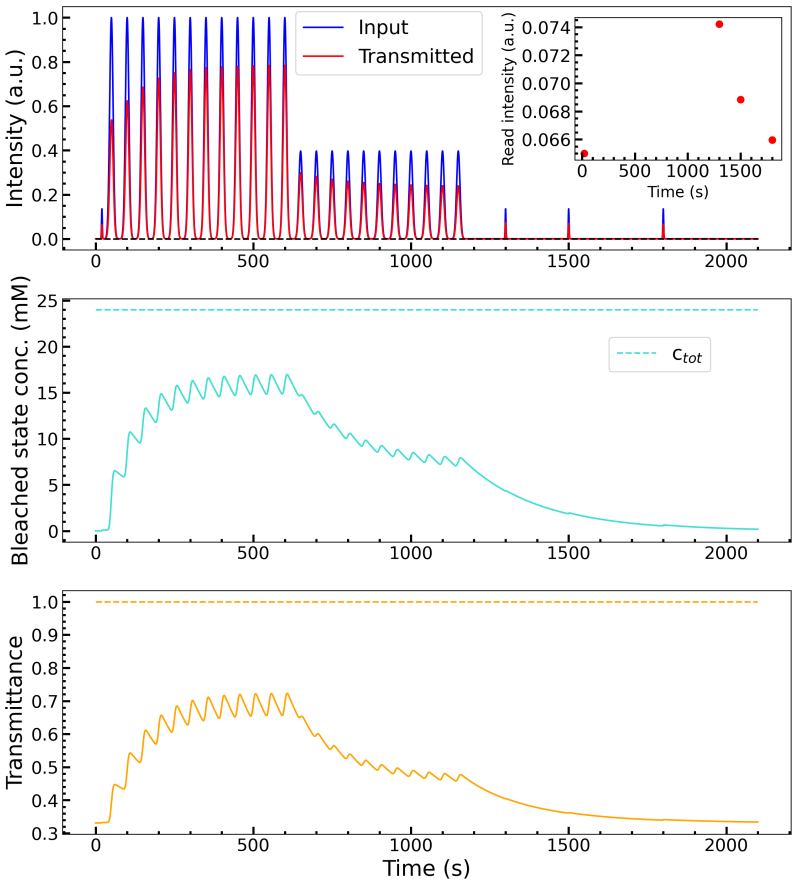

Figure 18: Results from the numerical solution of Eq. 8, illustrating a read/write memory. See Table 1 for parameters used. See text for details.

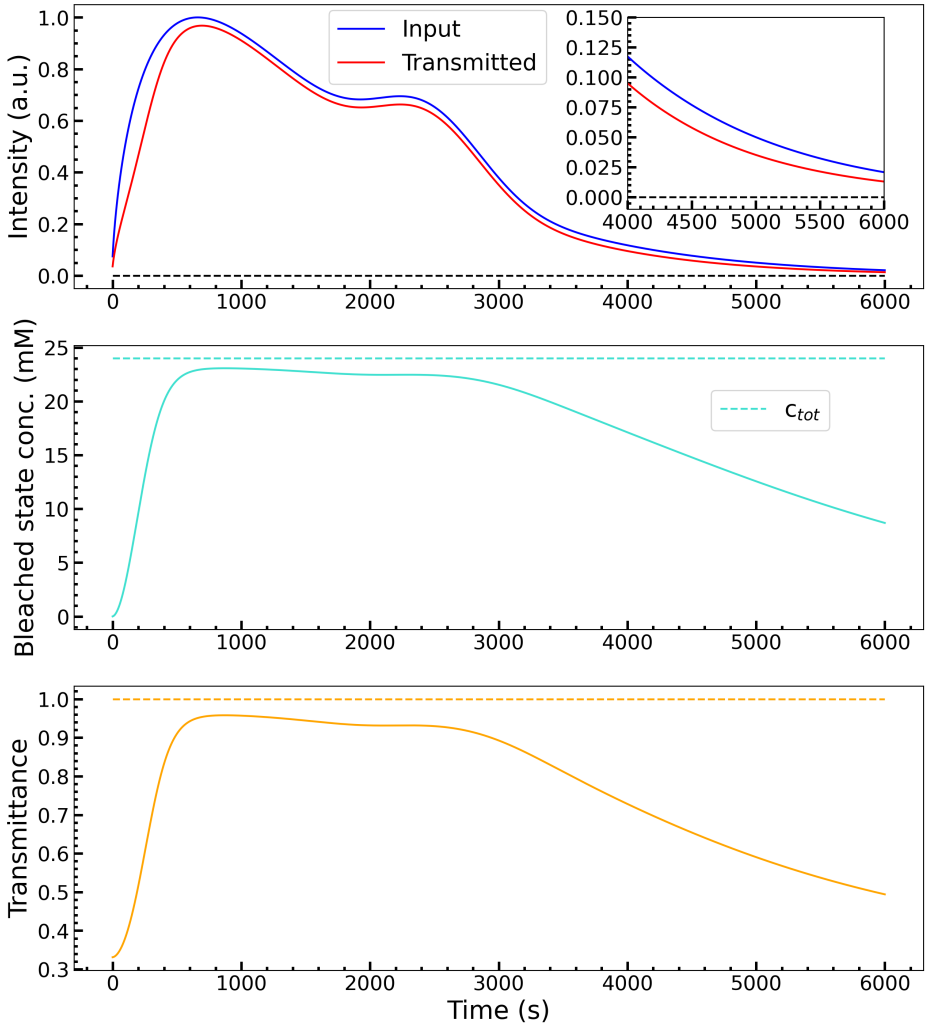

Figure 19: Results from the numerical solution of Eq. 8, illustrating a dynamic memory. The inset shows the last 2000 s intensities in greater detail. See Table 2 for parameters used. See text for details.

4.1.2 Experimental results

Dye on sapphire Figure 20 shows time-resolved transmission spectra of a AP-048 dye/polymer film (5 mM solution) deposited on sapphire by drop casting. The dashed line shows the transmission of a blank sapphire sample, while the full black line ("Dark") shows the film sample transmission before any bleaching. After recording the "Dark" spectrum, the sample was bleached for 7 minutes at intensity 500 using the Solar Simulator 633-711 nm LED (corresponding to $\sim$ 1.2 mW/cm^2). $\Delta t = 0$ is defined as the time when the Solar Simulator LED is turned off. Hence, the blue curve shows the transmission of the sample 1.5 minutes after finished bleaching. The spectra at successively later times, show the progression of sample transmission as the dye recovers its color. The transmission was measured using the integrating sphere of the Bentham setup; due to the transfer time between the two setups, the earliest Δt available is 1.5 minutes. All spectra are normalized to the integrating sphere signal at 100% transmission conditions.

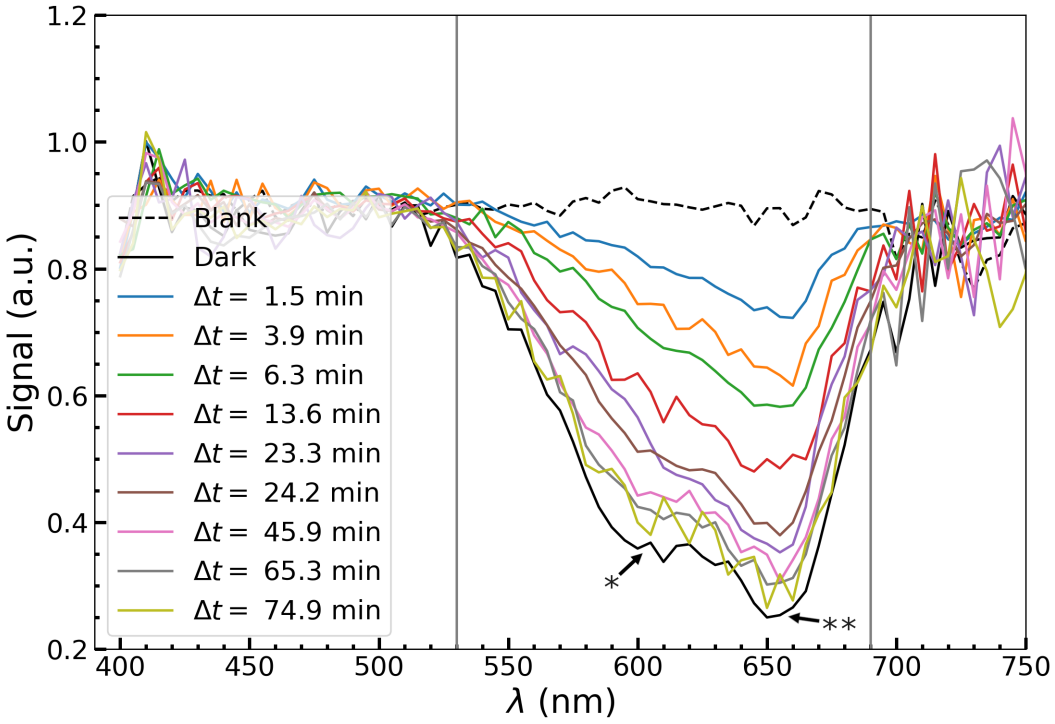

Figure 20: Time-resolved transmission spectra of AP-048 dye/polymer film (5 mM solution) drop cast sample 2 on sapphire. The dashed line shows the transmission of a blank sapphire sample, while the full black line shows the film sample transmission *before* bleaching. The remaining spectra in the Figure, show how the sample progressively becomes opaque again, *after* bleaching in the Solar Simulator. $\Delta t = 0$ is defined as the time when the Solar Simulator LED is turned off.

In order to extract the rate constant k of the dye color recovery (i.e. back-reaction rate), the transmission signal was averaged over the interval [530, 680] nm (gray, vertical lines in Figure 20), for each recorded spectrum and plotted as a function of time. A single exponential function was fit to this data, giving an estimate of the back-reaction rate k.

In comparing drop casting with spin coating, it was observed as a general trend, that spin coated films exhibited a much slower back-reaction than drop cast films. Similarly, thinner films regained color slower than thicker films deposited using the same method.

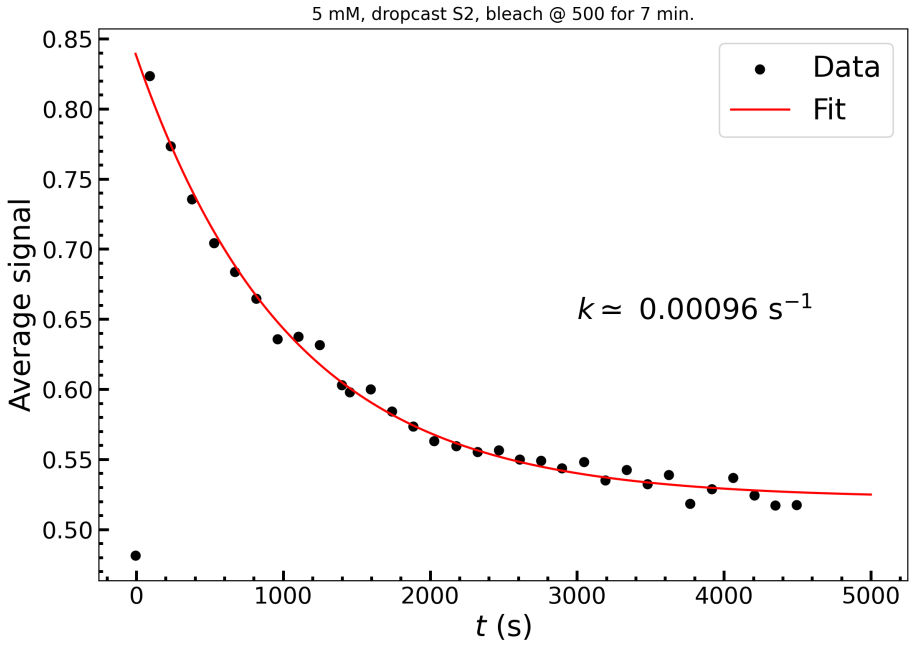

Figure 21: Mean drop cast sample 2 transmittance as a function of time (dots) and single exponential fit (red line). The time constant k of the fit is ∼1E-3 s^{-1}. The left-most data point is the transmittance before bleaching.

A comparison of extracted time constants k for three different film samples are shown in Table 3. The decay rate in toluene solution is included for reference (courtesy of Abbey Meprathu Philip). After annealing at 70°C for 20 minutes, the measurements were repeated and the decay rate time constants determined again (given as k' in Table 3). The annealing step seemingly decreased the decay rates of the two drop cast samples to values more in line with that of the spin coated sample, while the spin coated sample decay rate itself did only change very slightly. This effect could be explained by the heating allowing the drop cast samples' polymer matrix to relax, adopting a structure more similar to the one attained by spin coating.

These results confirm that the dye as deposited in a polymer matrix retains its reversible photobleaching properties, at least qualitatively.

Table 3: Film thickness and back-reaction rate k for a few 5 mM AP-048 dye samples (deposited on sapphire unless otherwise noted). Film thickness was measured using the DekTak Profilometer. k' denotes the back-reaction rate after 20 minutes annealing at 70°C.

Sample	**Film thickness** (μm)	k (s^{-1})	k' (s^{-1})	k'/k
Solution (toluene)	-	4.3E-3	-	-
Spin coated (1500 rpm)	2-3	6.1E-5	5.8E-5	0.95
Drop cast 1	9-10	3.9E-3	1.2E-5	0.003
Drop cast 2	2-5	1.0E-3	1.8E-5	0.019
Drop cast on NWA	?	2.1E-3 - 1.6E-3	-	-

Dye+NWA solar cell Since a too slow recovery rate would lead to unwieldy measurements times, the drop casting method was used to deposit the dye/polymer mixture on the NW array solar cell.

Figure 22 shows the EQE of a InP NW array device with (red curve) and without (black curve) a drop cast covering layer of the 5 mM AP-048 DASA dye suspended in a polymer (PAMS) film. The dye film significantly alters the absorption profile of the NW device. As expected, the change in EQE closely resembles the absorption profile of the dye (see Figure 10 and blue curve in Figure 22).

In order to investigate the bleaching dynamics of the combined system, a simple script was written to control the illumination of the G2V Pico Solar Simulator. For the results presented here, two such long term measurements are of relevance. The first data set has been nicknamed "Pyramids" and the second "Pulses".

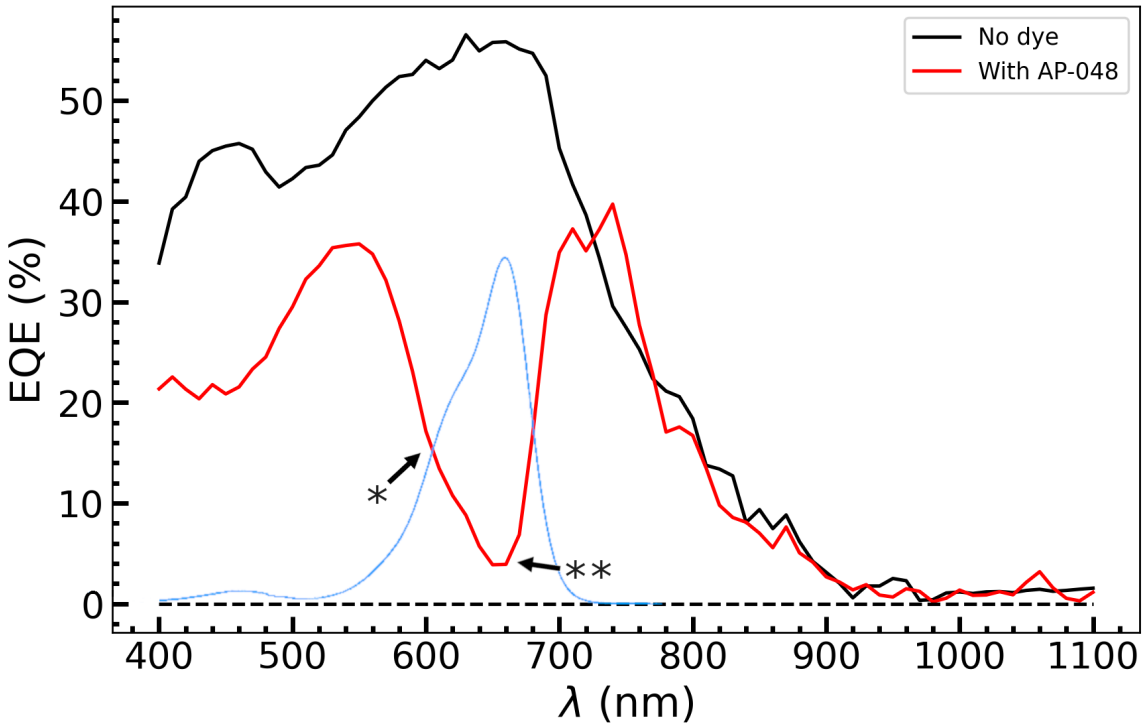

Figure 22: Addition of AP-048 molecular dye on an InP NWA has a marked effect on the external quantum efficiency of the NW device. The change in EQE should be compared to the AP-048 absorption spectrum, included in blue (Figure 10).

"Pyramids" data set This measurement was conducted to investigate the basic functionality and long-term durability of the dye+NWA system. The sample was illuminated at different intensities, while the current was measured simultaneously.

Figure 23 offers an overview of the results: 14 "blocks" of different average current, corresponding to the different illumination intensities used. Please refer to Appendix B for the exact illumination times and intensities used.

The intensities 150, 350 and 550 are repeated four times each, while the 1000 intensity block is only repeated twice, forming two "pyramids". Each block is separated by a period where the light is completely turned off, with the two "pyramids" being separated by an significantly longer light-off period. Each block consists of six high-intensity periods

interspersed by low-intensity periods. Using the read/write terminology introduced above, one can interpret the high intensities as the *write* intensity and the low intensity as the *read* intensity. While the *write* intensity is changed from block to block, the *read* intensity is always the same. Based on the simulation results presented above, it is expected that the current will increase to a maximum during the *write* period, representing the equilibrium between the bleaching and back-reaction rates for the intensity in question. In the subsequent *read* period, corresponding to a much lower intensity, the current is expected to exponentially decay to a new equilibrium value as many of the previously bleached molecules regain their color. Assuming that the *read* intensity is low enough, the exponential decay rate of the current in this period should closely resemble the decay rate in absence of any illumination. Hence, by fitting to the *read* intensity data, an estimate of the back-reaction rate k should be obtained.

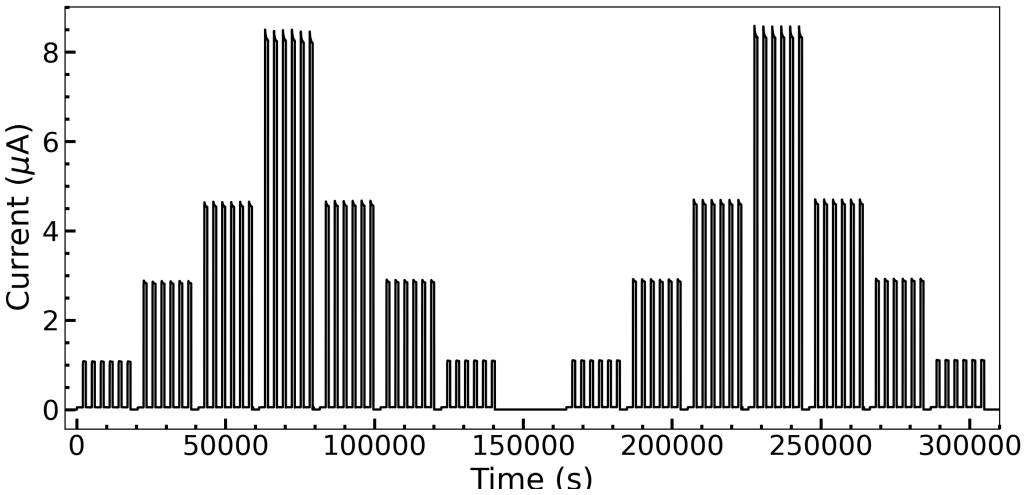

Figure 23: Photocurrent from the dye+NWA combined system as a function of time under different illumination intensities. The light source was the 633-711 nm LED of the Solar Simulator. See Appendix B for the experimental parameters used.

As the representative Figure 24 shows, there are several different effects to be disentangled. Figure 24 *top* shows an overview of the first illumination set; the numbers in red show the input light intensity (in Solar Simulator units). A higher intensity generates a larger current in the solar cell, which is expected. Figure 24 *middle* shows the high-intensity part, which features two different exponential trends in opposite directions: one quick up to a maximum current I_{max}, and one slow which reduces the current again over time. These effects are more clearly seen in Figure 25, which shows all of the high-intensity (i.e. *write* intensity) periods. Finally, Figure 24 *bottom* shows the low-intensity region, featuring a decay of the current over time.

In order to investigate the durability and repeatability of the dye+NWA system, it is helpful to inspect the sample response for each illumination intensity as a function of the number of repetitions of that intensity. In Figure 25, this is done for the high-intensity periods. As the Figure shows, the maximum current reached for each intensity increases with the number of repetitions, reflecting a cumulative bleaching of the dye over the course of the measurement. For the 150 intensity graph, I_{max} is reached after about 150-175 seconds. Beyond this point, the current decreases slowly. The same trends are

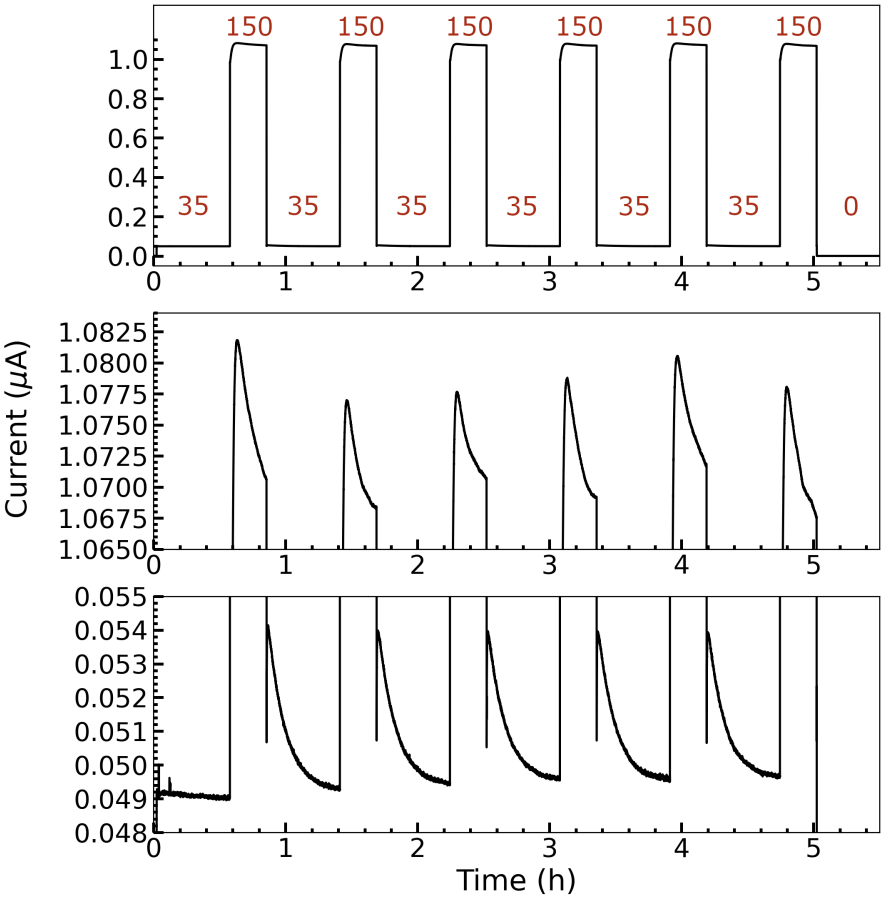

Figure 24: The first block of Figure 23 in greater detail. The numbers in red represent the Solar Simulator illumination intensity (see Table 5 for a conversion table). *Top:* Overview over the first illumination set. *Middle:* zoom-in on the high-intensity region. *Bottom:* zoom-in on the low-intensity region.

found for all high-intensity plots in Figure 25, with the difference that the time to reach I_{max} decreases with increasing intensity. This could indicate that the first part of the traces is related to the bleaching of the dye, as a higher intensity will bleach a set number of molecules faster than a lower intensity.

The second part of the traces, i.e. where the current decreases, cannot be explained by the photophysics of the dyes, as there is no mechanism by which the molecules would regain their color under constant illumination. The only exception would be if the illumination itself raised the sample temperature, thereby shifting the bleaching/back-reaction equilibrium. This was investigated by studying the sample surface using an IR camera. The sample temperature was found to be constant within ± 0.8°C at the highest intensity used, over an illumination time equal to that used in the measurements. Hence, sample photoheating is unlikely to be the cause of the effect in question.

Another way to approach this question, is to note that based on the cumulative bleaching observed, one would expect that the magnitude of current decrease from I_{max} likewise would be a function of the number of repetitions, if the effect indeed was related to the dye photophysics. In Figure 26, this difference in current, termed ΔI_{max} (see Appendix C for an exact definition), is plotted for the different illumination intensities. For the high intensities, the Figure shows ΔI_{max} to be purely a function of illumination intensity, and

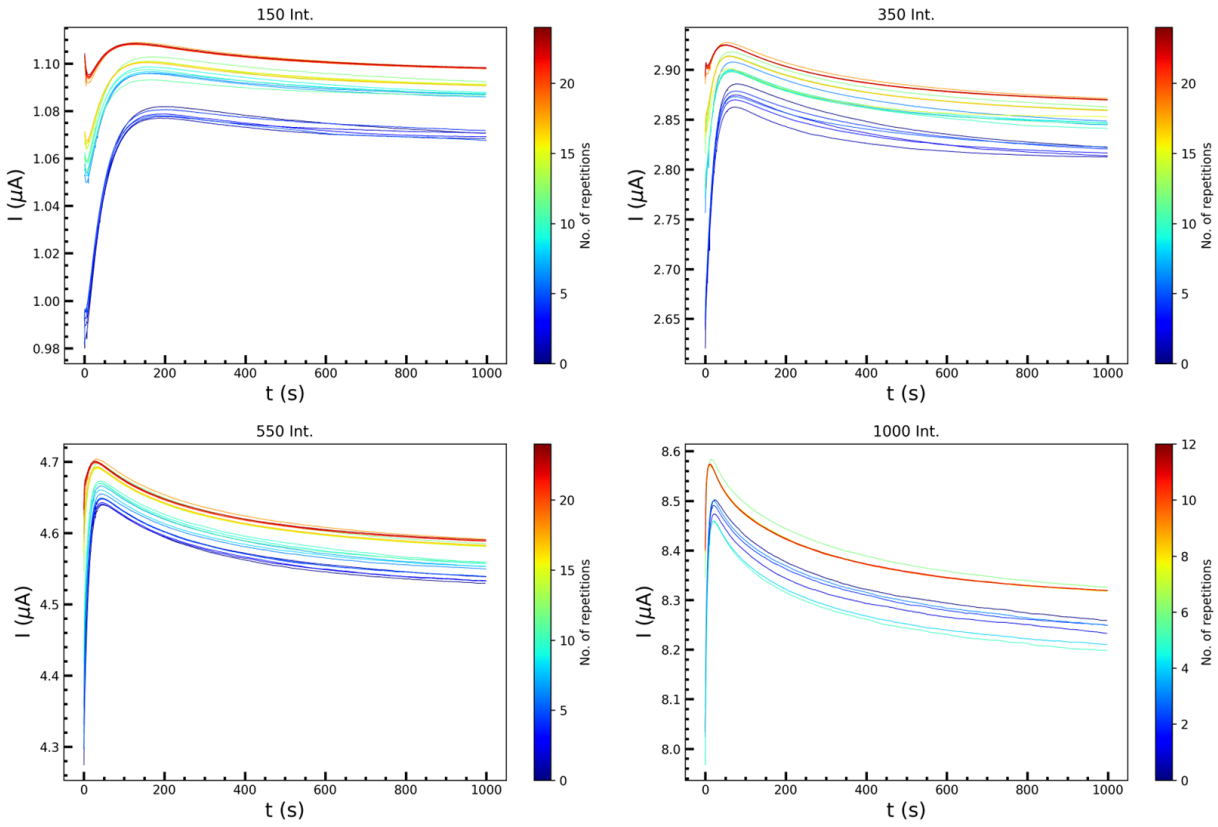

Figure 25: The high-intensity periods in the "Pyramids" data set as a function of time and number of repetitions. The subfigure titles denote illumination intensity (see the Table in Appendix B for intensities in units of mW/cm^2).

independent of the number of repetitions. This strongly indicates that the effect is not related to the dye molecules.

Instead, the effect could be related to either the light source or the NWA. Using an Si detector, the emitted optical power from the relevant Solar Simulator LED at "Intensity 1000" was studied over time. The results are presented in Appendix D, and shows some systematic variations which are about a factor 10 smaller than the magnitude of the observed effect, meaning that the light source variance does not offer the full explanation. Hence, the most likely hypothesis seems to be that the major part of the effect originates from the NW array solar cell itself, possibly being caused by a charge build-up somewhere in the device.

Returning to Figure 26, one can note that the *read* intensity ΔI_{max} ("35 Int."; yellow dots), decreases with increasing number of repetitions. Following the above line of reasoning, this indicates that the decaying-part of the *read* intensity periods is related to the dye photophysics. Figure 27 shows all *read* current traces (except for those in Figure 29) as a function of the number of repetitions.

Each of these traces is preceded by a 1000 s high-intensity *write* period (see Figure 24), and the expectation is that the current will decay exponentially over time during the *read* period. This is indeed the case, as Figure 27 shows. However, the range over which this decay happens, grows smaller with increasing number of repetitions. To this, three different, complementary explanations can be offered. Firstly, it could be that not all dye molecules have time to recover during the light-off periods, giving rise to a cumulative

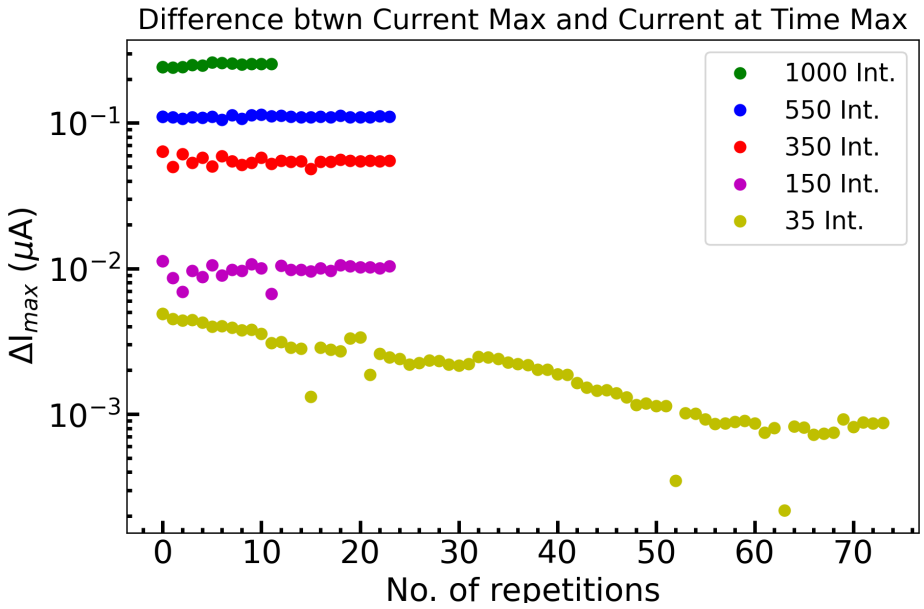

Figure 26: ΔI_{max} (see Appendix C) for the illumination periods in the "Pyramids" data set as a function of the number of repetitions.

but still, given enough time, reversible bleaching. Secondly, some dye molecules will likely become permanently photobleached during the *write* periods, leading to a cumulative, irreversible bleaching. Thirdly, since the dye was deposited by drop casting, it is possible that the structure of the polymer matrix in which the dye molecules are suspended changes over time. If such structural changes increase the sterical constraints on the molecules, the back-reaction rate k would be decreased.

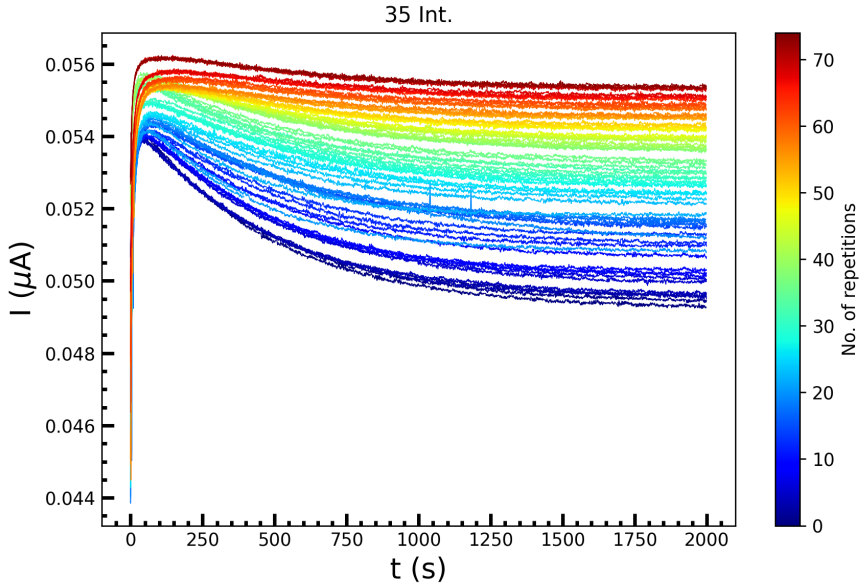

Figure 27: The low intensity (i.e. *read*) periods in the "Pyramids" data set as a function of time and number of repetitions.

During the first few seconds, the traces in Figures 27 undergo a comparatively speaking very rapid change in current; this effect could be caused by lamp anomalies when switching intensity and/or a capacitive response from the NWA.

By fitting single exponential functions to the identified relevant parts of Figures 27 and 25 (i.e. fits corresponding to the red lines in the Figure in Appendix C), the time constants k characterizing these trends were extracted. The absolute value of these are plotted in Figure 28 as a function of the number of repetitions. The data points $> 10^{-2}$ s^{-1} correspond to the *write* intensity fits, while the data points for which $|k| < 10^{-2}$ s^{-1} belong to the *read* intensity fits. The k-values extracted from the *write* intensity fits thus report on the rate of bleaching, which should be a function of the illumination intensity. Some of the fits were not successful, explaining the presence of outliers in Figure 28, especially towards the end of the measurement. In spite of this, the general and expected trend that higher intensity leads to faster bleaching is visible as the "pyramid"-structure of the data set is reproduced in the distribution of the time constants.

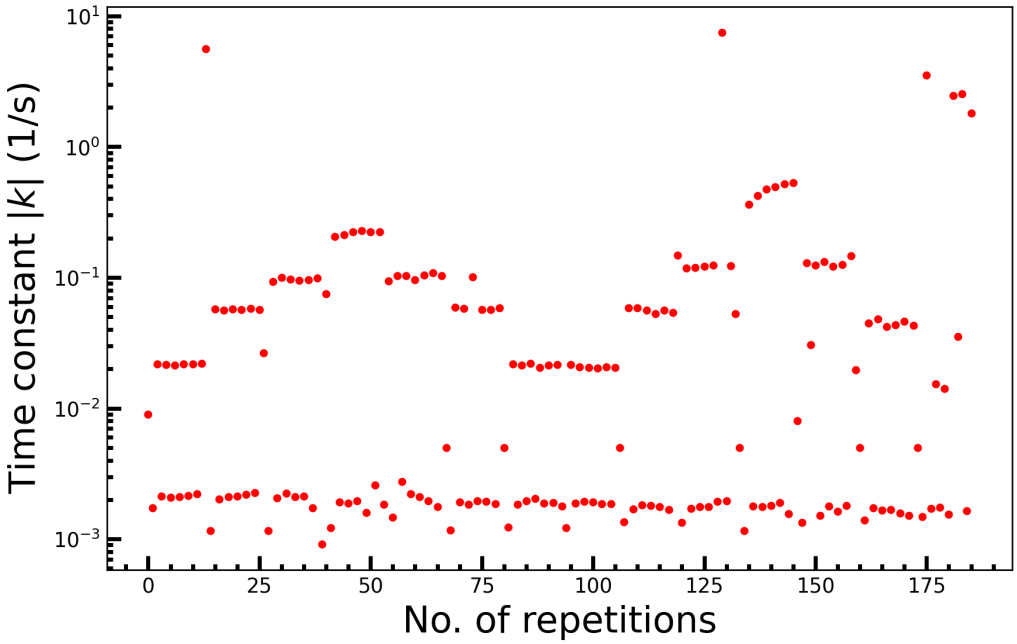

Figure 28: Time constants k (absolute values) extracted from fits to the bleaching and recovery decays in the "Pyramids" data set.

Also of interest are the back-reaction rate constants extracted from the low-intensity periods, as these should be directly comparable to the dye-on-sapphire measurement results. From Figure 28, $k \simeq$ 2.1E-3 s^{-1} at a low number of repetitions, while $k \simeq$ 1.6E-3 s^{-1} towards the end of the data set (ignoring outliers), for the *read* fits. Two observations should be made here. Firstly, that the average back reaction rate lies in-between those determined for the drop cast dye-on-sapphire samples before annealing (see Table 3), which strongly indicates that the dye film behaves similarly regardless of whether it has been deposited on sapphire or a NW array solar cell, and which furthermore offers a rough estimate of the thickness of the film deposited on the NW array. Secondly, that the measured back-reaction rate decreases roughly linearly with time. The back-reaction rate k should be independent of the absolute number of photoactive dye molecules, and

permanent photobleaching can thus not explain the phenomenon. Instead, one possibility is that the film properties change over time, which in turn could affect the photophysics of the dye molecules embedded within.

Figure 29 shows the special "0 → 35" *read* current traces which occur at the very start of each *write* block. Hence, there are only 14 such traces, corresponding to each of the 14 blocks in this measurement. As such, they provide highly valuable information.

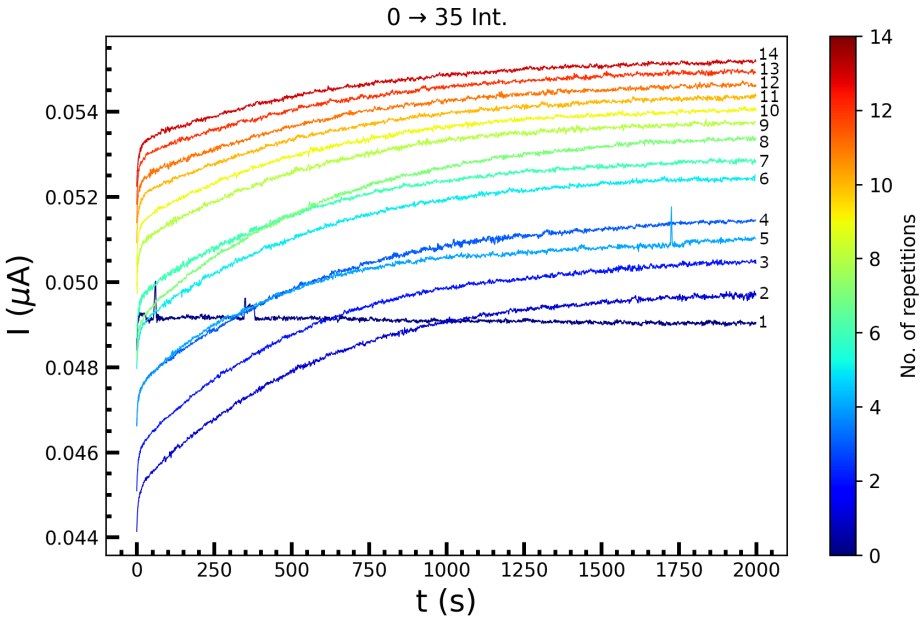

Figure 29: The 14 *read* intensity periods preceding each of the 14 *write* intensity illumination sets in the "Pyramids" data set (Figure 23).

Each "0 → 35" trace is preceded by a 2400 s light-off period, except for traces numbers 1 and 8. Trace number 8 is preceded by the long dark period of 24000 s separating the two "pyramids" (see Figure 23), while trace number 1 is not preceded by any dark period, but instead by the ambient light conditions during the preparation of the measurement. Consequentially, the dye molecules are in some partially bleached state at the start of trace 1. This first trace is almost constant, but does nonetheless decrease very slightly with time, which indicates that the *read* intensity is only slightly lower than the average ambient light conditions during the measurement preparation. After trace 1, the first *write* block (at intensity 150) occurs, followed by 2400 s of darkness during which the molecules will successively regain their color. This is followed by trace 2, which starts out at a lower current than trace 1, which is expected since trace 1 was not preceded by a light-off period. At $t = 2000$ s, trace 2 reaches a slightly higher current than trace 1. That trace 2 is able to reach a higher current could at least in part be due to permanent photobleaching caused by the high-intensity *write* block. Trace 3 both starts out at and reaches a higher current than trace 2, which is consistent with the permanent-photobleaching explanation. This trend generally repeated for the traces in Figure 29; however, traces number 5 and 8 break the pattern.

Trace 8 starts out at a lower-than-expected current, but this is in line with the extended light-off period preceding this trace, which would allow a larger-than-usual portion of the molecules to regain their color. That trace 8 reaches the "expected" current between traces

7 and 9 is in fact consistent with this interpretation, due to the permanent photobleaching caused by the last *write* block before the 24000 s light-off period. In these ways, trace number 8 serves as a rather strong indication that the results presented here do report on the actual dye photophysics.

The permanent-photobleaching explanation fails to explain trace number 5. As this is the first "$0 \rightarrow 35$" trace after the first intensity 1000 *write* block, it could be tempting to associate the anomaly with some sort of "shock" effect caused by this very high intensity. But since no corresponding effect is seen in trace 12, there is no real case for that hypothesis.

That the traces successively crowd together with increasing number of repetitions, could be an effect of that the total number of photoactive molecules diminishes over time, such that the absolute number of permanent photobleaching events also decreases over time.

One should note that the *write* illumination intensities and times used in the "Pyramids" data set are excessive relative to the amount of deposited dye molecules. Mostly this means that the bleaching equilibrium is attained in just a few seconds for most of the *write* periods, which in spite of this go on for 1000 seconds each. But as a major motivation for this measurement was to test the durability of the combined dye+NWA system, these excessive *write* periods are still of relevance. The results presented in Figure 25 allow us to say that even after driving the system this strongly, the same *write* intensity will still affect the system in the same way, to within $\sim 3\%$.

"Pulses" data set Here, we will focus on a specific selection of the "Pulses" data set, corresponding to pulse sets numbers 10-14 in 4b in Appendix B. This selection is presented in Figure 30, and consists of five identical pulse sets, separated by 1000 s light-off periods. Each pulse set consists of 20 short pulses at intensity 150. This measurement was performed in order to investigate the behavior of the dye+NWA system under pulsed illumination, and as a further test of the repeatability of the bleaching process.

Figure 30a shows an overview of the five pulse sets, and Figure 30b shows the top part of first (black) and last (red) of these pulse sets. The blue dashed line indicates the maximum value reached in pulse set 5. For a given pulse set, each consecutive high-intensity pulse generates a slightly larger current, slowly trending towards a plateau. This behavior is qualitatively very similar to the simulation results in Figure 18, corroborating the interpretation of the experimental results as being caused by the progressive bleaching of the dye layer.

Comparing the maximum signal reached during the first pulse set to the corresponding value in the consecutive pulse sets (Figure 30c), shows that any variations are smaller than 0.2%. In contrast to the "Pyramids" data set, no distinct signs of permanent photobleaching are seen here. Since the total illumination time at high intensity in the pulsed measurements is much shorter than in the "Pyramids" measurement, a much smaller permanent photobleaching effect would indeed be expected.

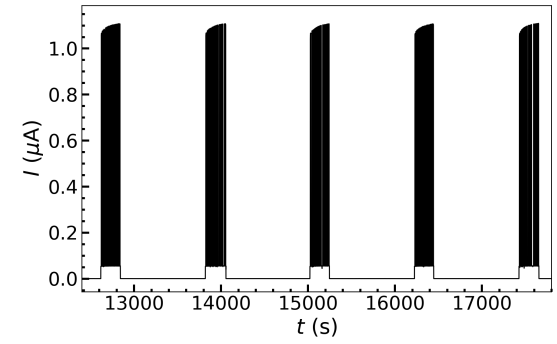

(a)

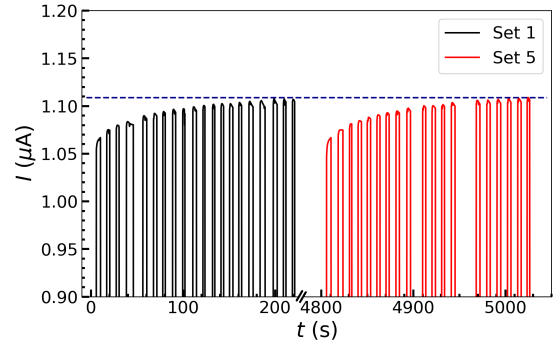

(b)

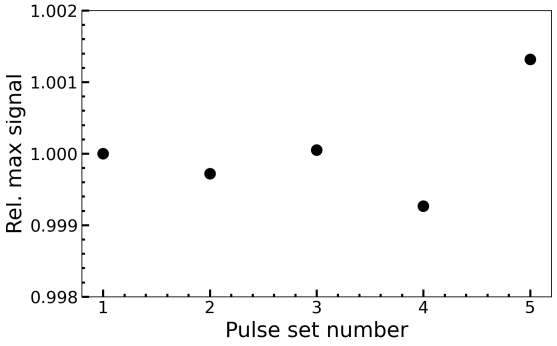

(c)

Figure 30: (a) Overview of the five identical pulses sets, corresponding to sets 10-14 in Table 4b in Appendix B. (b) Comparison between the first and fifth of the pulse sets. (c) Maximum signal attained for each pulse set, normalized to set no. 1.

High-concentration dye film As the final device requires NW-NW distances of ~ 2 μm [9], and hence a significant dye absorption at this film thickness, it was of relevance to probe the limits of increasing absorption through increase of dye concentration. To this effect, a 24 mM AP-048 solution (5%-wt dye-to-polymer) was used to spin coat sapphire samples at various speeds. As before, the film thickness was measured using a profilometer, and the transmission spectra of the samples recorded using the integrating sphere.

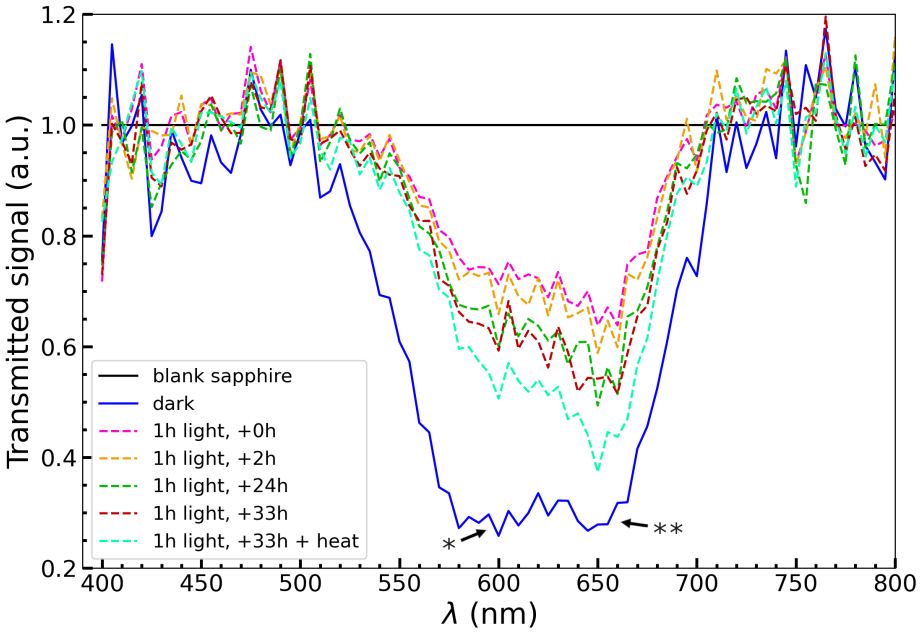

Figure 31: Time-resolved transmission spectra of a high-concentration AP-048 dye/polymer film drop cast on sapphire. The full blue line shows the film sample transmission before any bleaching. The dashed spectra show the sample transmission as it changes over time after 1 h illumination in the Solar Simulator at intensity 1000. All spectra are normalized to the transmission spectrum of a blank piece of sapphire.

Figure 31 shows the transmission data for an $l \simeq 1.5$ μm film spin coated at 8000 rpm; the black curve shows the transmission for a sapphire sample without any film and the full blue curve shows the transmission for the $l \simeq 1.5$ μm film sample after minimal light exposure. As is seen, a major change in transmittance was achieved with the 24 mM solution. However, the transmission profile (blue curve) in the Figure differs from those of the 5 mM samples shown in Figures 20 and 22. In these previous results, the spectral feature denoted by $*$ is smaller than the main peak (denoted $**$); in Figure 31, the two spectral features are of equal size, and have more or less merged. This change in absorbance is indicative of the dye molecules aggregating; a well-known possible effect of high concentration solutions [31]. Among other things, such aggregation can affect the reaction kinetics of the molecules, making it a possibly unwanted effect in this context.

A measurable change in the transmission spectrum was first achieved after high intensity illumination at extended duration. The pink, dashed curve in Figure 31 shows the transmission after 1 hour illumination at 2.4 mW/cm^2, i.e. the maximum intensity used in this work. After this bleaching, the recovery of the dye color progressed much slower than would be expected from the 5 mM sample. Based on Figure 31, the recovery had saturated 33 hours after the illumination (dashed red line). At that point, the sample

was annealed in the same way as described above (i.e. heated to 70°C and kept at that temperature for 20 minutes). The dashed cyan line shows the transmission after heating, which has decreased markedly as compared to either the 24 hour or 33 hour mark before heating. This is in qualitative accordance with the temperature dependence of the back-reaction rate k; i.e. that color-recovery should progress more rapidly at elevated temperatures.

Similar results were retrieved for both 10 and 15 mM dye solutions. The extremely slow bleaching and back-reaction rates disfavored the use of > 5 mM dye solutions in this context.

4.2 NW Opto-Electronics

In this Section, studies of a number of different InP + InAs NW devices are presented, where an InP NW is used to either enhance or diminish the conductance of an InAs NW, *via* a field-effect gate (see Figure 7 for a schematic of the gate structure). The results presented in this Section, hence pertain to the subsystem highlighted in Figure 32. The assembling of the devices, which were provided by Joachim Sestoft and Jesper Nygård, entailed the accurate placement of single NWs using a micromanipulator. The gate oxide consists of 15 nm of HfO_2, while the gate metal is the same Ti/Au alloy used for the leads contacting the NWs.

The devices where studied in the Unisoku setup, primarily by OBIC, but also by stationary, power-dependent illumination. The results presented here pertain to devices on two different samples: labeled PT7 and PT8. For clarity, the SEM images and OBIC scans of each device will be presented as subfigures in the same Figure. The SEM images of each device were provided by Joachim Sestoft.

All InP NWs where p-i-n doped, with the p-segment always coinciding with the "top" of the NW, i.e. the segment closest to the Au-particle left over from the NW growth. As stated in Section 1, "n/p-gated" denotes devices where the n/p-segment of the InP NW is connected to the InAs gate.

The circuit diagram in Figure 32 holds true for the results presented in this Section; in some cases the InP symbol denotes two InP NWs connected in series. The only other exception is the PT7-12 device, for which the measured current is simply the photocurrent generated by the single InP NW which constitutes the entirety of that device. See Appendix E for the experimental parameters pertaining to the OBIC scans presented in the following.

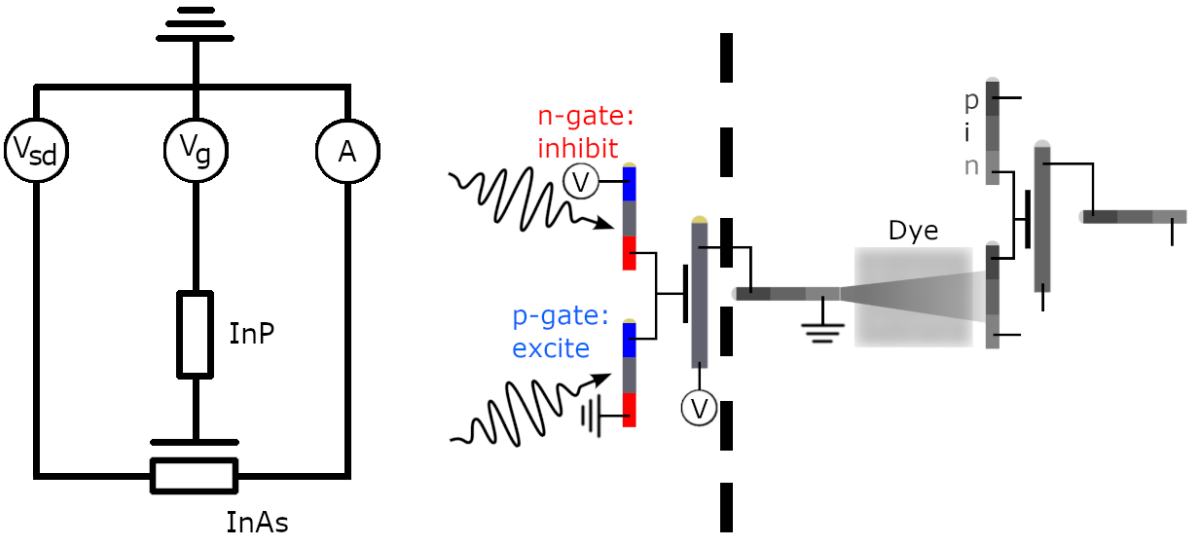

Figure 32: Left: generalized circuit diagram for the measurements presented in this Section. Right: the part of Figure 3 these results pertain to.

4.2.1 PT7: device 12 (InP NW)

In this Section a single InP NW is studied using OBIC. This serves two purposes: (1) to test and exemplify the basic functionality and limitations of the OBIC setup, and (2) to set a scale reference for relevant distances and current magnitudes. Figure 33a shows the SEM image of PT7-12: a single InP NW, while Figure 33b shows an OBIC scan approximately centered on the NW. The NW is unbiased, and all produced current is pure photocurrent. The exposed length of the InP NW is ~ 1.44 μm, and the FWHM of the photocurrent spot is approximately 1 μm. The OBIC scan appears more or less circular, and it is not possible to resolve the shape of the NW. The total incident optical power was $P_{LD} \simeq 10$ nW, and the maximal photocurrent produced by the InP NW was ~ 50 nA.

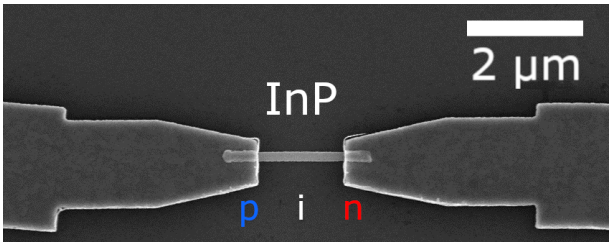

(a)

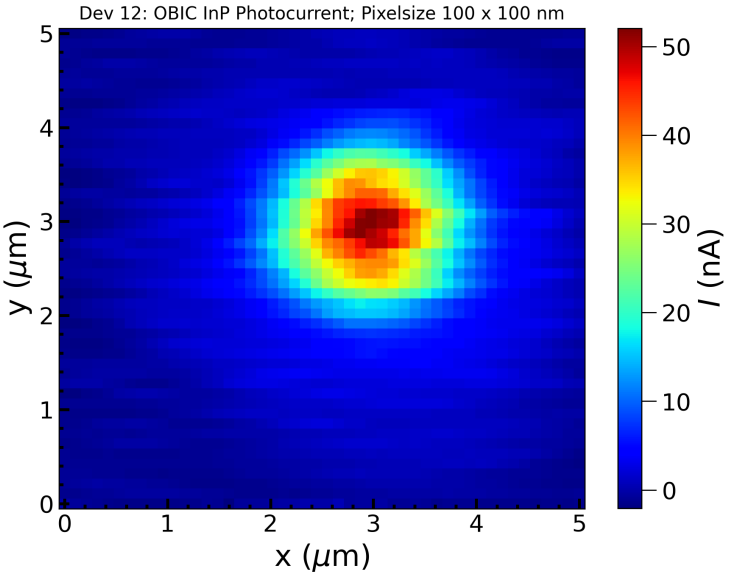

(b)

Figure 33: (a) SEM image of device PT7-12; a single InP NW. (b) OBIC scan of PT7-12; $P_{LD} = 10$ nW. The InP NW is located at the center of the high-current region.

This result confirms that the Unisoku/OBIC setup works as intended, and demonstrates that a single NW, in spite of its high aspect ratio, will appear as a more or less circular feature in the OBIC scans presented here.

The optical path length of the reflected light from the sample surface to the CMOS camera was not the same as the optical path length of the LD light from the fiber incoupling to the sample surface. In other words, it was not possible to simultaneously

focus the LD on the sample and having the sample surface in focus in the camera view. But by iteratively focusing each component and comparing the camera view with the photocurrent induced in the InP NW, it was possible to map the position of the focused LD beam to the view of the sample surface seen through the camera. The two ring markers in Figure 34 gives an example of such a mapping.

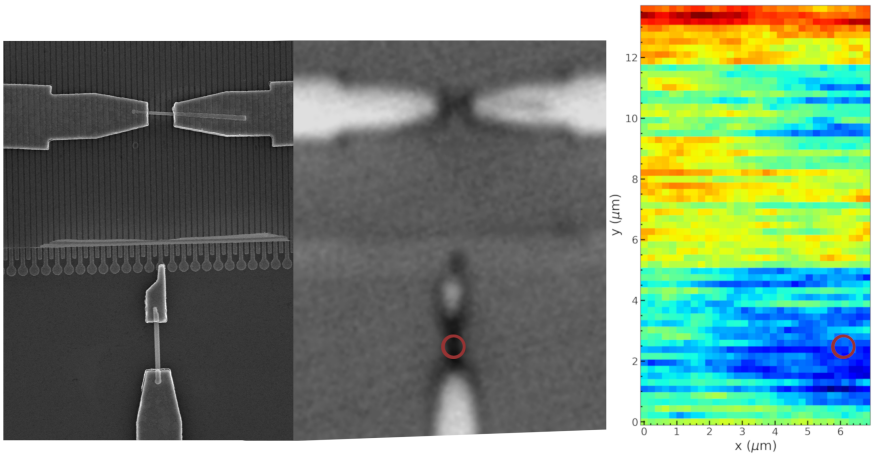

Figure 34: Device PT7-3 imaged by SEM (left), optical microscopy (middle), and OBIC (right). The ring marker in the two right-most images show an example of the determined corresponding positions in the microscopy and OBIC imaging modes.

4.2.2 PT7: device 3 & 9 (n-gate InP/InAs)

In this Section, we will explore the device PT7-3 imaged in Figure 35; an n-i-p doped InP NW with its n-side connected to the field-effect gate beneath the InAs NW. This device type fills a role similar to the inhibitory sub-component of the neuromorphic component discussed in Ref. [13]. The device is connected to the setup as shown in Figure 32. At first, the behavior of the device under non-specific illumination using the LED is tested, and next OBIC scans are performed to investigate the device using more precise illumination.

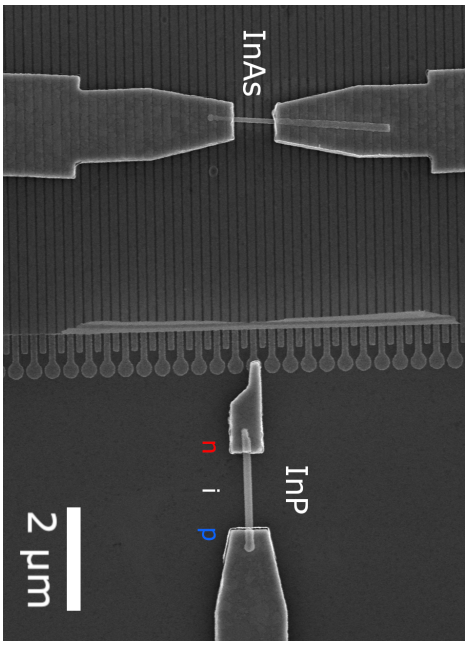

Figure 35: SEM image of device PT7-3.

Next, PT7-9 (see Appendix F), a device with the same design as PT7-3, is investigated using power dependent measurements. In these, first the InP NW is selectively illuminated by the LD, and the optical power P_{LD} stepped from $0 \rightarrow 10^{-3} \rightarrow 0$ W in discrete steps. The InAs conductance is measured for each value of P_{LD}. The measurement is then repeated with the InAs as the illumination target. The power dependent measurements are mainly performed to provide an unambiguous distinction between the two NWs, but also to probe for memory effects in the device.

Figure 36 shows the measured InAs current at $V_{SD} = V_G = 0$ when the Unisoku LED is turned on ($t \simeq 25$ s) and then off ($t \simeq 38$ s) again. The current drops when the device is illuminated, and recovers when the light is turned off, with the current recovery featuring both a quick and a slow component. Note that there is a non-zero InAs current even when the light is turned off and no bias is applied, contrary to expectations for an intrinsic NW. One possible reason for this could be differences in interface quality between the two InAs contacts, leading to a non-flat conduction band even at zero bias.

Figure 37 shows two OBIC scans stitched together at $y = 6.8$ μm; using $P_{LD} = 10$ nW. $V_G = 0$ V while $V_{SD} = 2$ mV, explaining why the current away from the device (~ 210 nA) is larger than the dark current in Figure 36. Two centra of current inhibition can be distinguished. The to-scale SEM image of the device is overlain and aligned with the axes of the OBIC heatmap. The positioning of the overlay along x and y is approximate and performed using the method explained above.

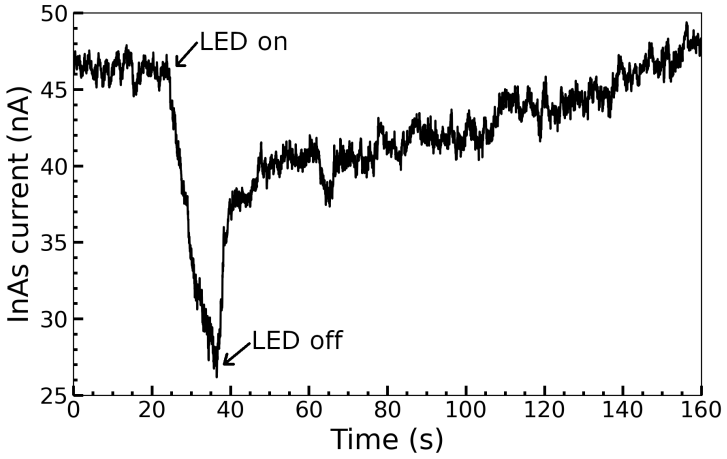

Figure 36: This Figure illustrates the extended time-delay of current recovery after illumination of device PT7-3 using the LED. V_{SD} =$V_G = 0$ V.

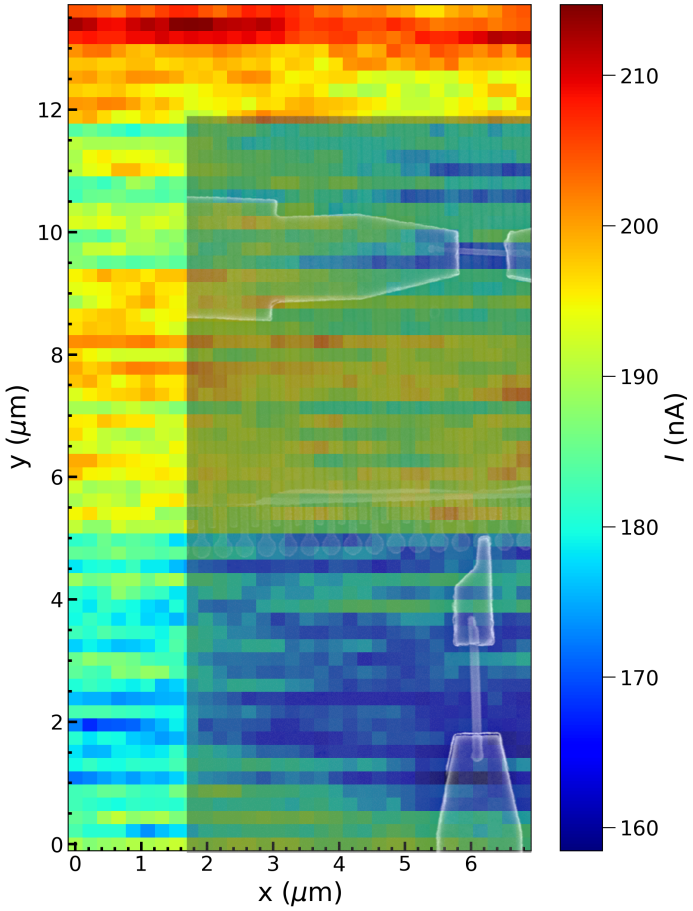

Figure 37: Image consisting of two stitched-together OBIC scans of device PT7-3. P_{LD} = 10 nW, $V_G = 0$ V and $V_{SD} = 2$ mV. Current is measured through the InAs NW (at $y \simeq 10$ μm); see Figure 32.

Figure 38 shows the results of the power dependent measurement on PT7-9. Each data point in the Figure corresponds to an InAs IV-sweep from V_{SD} = -5 to +5 mV. Each sweep took 62 s, and the time between each data point is approximately 30 s.The intensities were chosen to be linear in I_{LD}, explaining why the corresponding P_{LD} data

points are unevenly distributed.

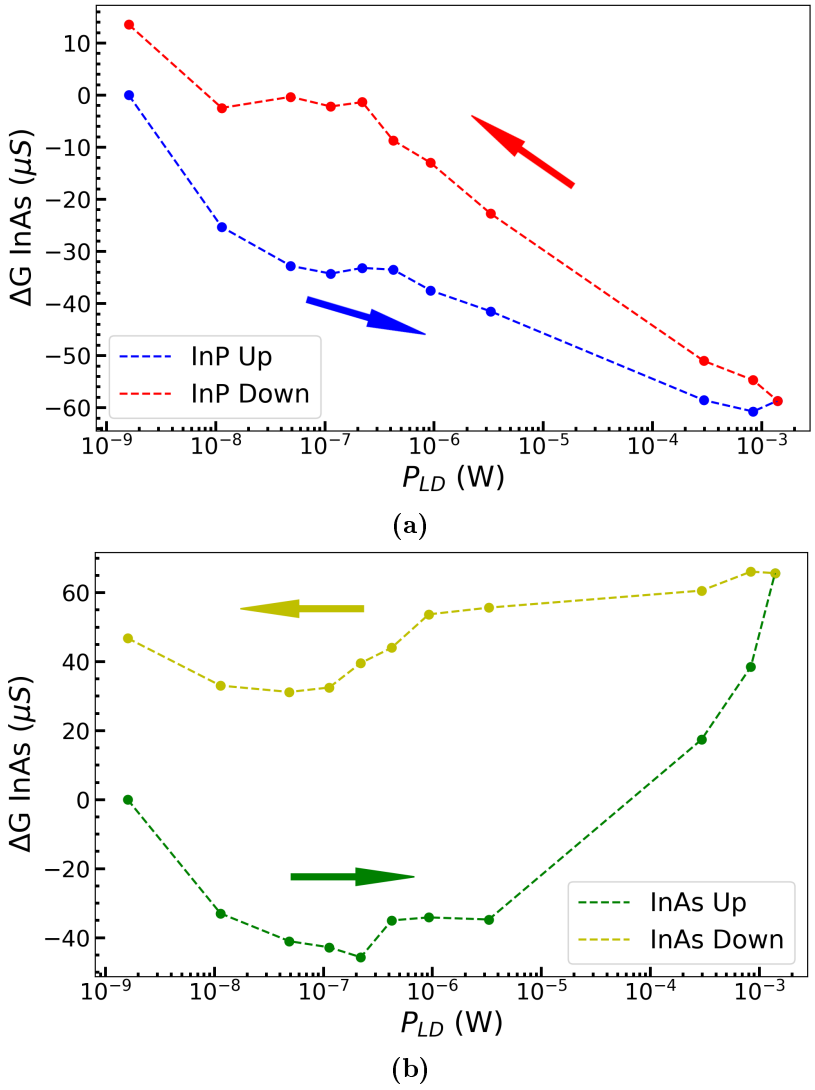

Figure 38: Power dependent measurements on device PT7-9: change in InAs conductance as a function of incident LD power. $V_G = 0$ V. Arrow direction indicates if P_{LD} is increased (right) or decreased (left). The measurement time for each data point is 60 s, and the time between each data point is $\sim$ 30 s. (a) Response when the InP NW is selectively illuminated. (b) Response when the InAs NW is selectively illuminated.

Subfigure 38a shows the relative change in InAs conductance ΔG as a function of P_{LD} when the InP NW is selectively illuminated. Based on the LD calibration curve (Figure 14), $P_{LD} = 1.6$ nW corresponds to the LD being turned off. When P_{LD} is increased (blue) from this minimum value, ΔG decreases and reaches -58 μS at $P_{LD} \simeq 1$ mW. When P_{LD} is stepped back down (red), ΔG increases again and returns to a value of $+15$ μS when the LD is turned off, i.e. somewhat above the original value.

Subfigure 38b shows ΔG as a function of P_{LD} when the InAs NW is selectively illuminated. As P_{LD} is stepped up (green), ΔG decreases until $P_{LD} \simeq 1$ μW; when P_{LD} is increased beyond this point, ΔG rises quickly and reaches $+63$ μS at $P_{LD} \simeq 1$ mW. As P_{LD} is then decreased (yellow), ΔG decreases as well, but remaining at high values relative to the green curve. When the LD is turned off again, $\Delta G \simeq +48$ μS, i.e. significantly

higher than the original value.

The OBIC scan (Figure 37) shows that the general inhibition of current upon illumination (Figure 36) exhibited by the PT7-9 device can be decomposed into two centra of inhibition. At $V_{SD} = 2$ mV and $P_{LD} = 10$ nW illumination power, a maximal decrease of current by about 50 nA is achieved ($\sim$24%). The distance between these centra of inhibition is ~ 7 μm, showing good agreement with the InP-InAs separation of ~ 7.1 μm, as evidenced by the to-scale overlay in Figure 37. That the InAs conductance decreases (more or less) monotonically when the InP illumination intensity is ramped up (Figure 38a), agrees with the expected FET gating of the device. For Figure 38b, the decrease of conductance at low intensities, followed by a large increase of conductance at higher intensities, is qualitatively similar to the NPC+PPC effect exhibited by the InAs NWs in Ref. [23] (discussed in Section 2.1.4). Furthermore, the significant memory effect (hysteresis) could corroborate this, since the trap states should have some non-zero lifetime.

However, the temporal characteristics of the memory effect seem to vary significantly between different InAs NWs, from a few milliseconds to several seconds [23]. Since the memory effect shown in Figure 38b persists for at least several minutes, it is not immediately clear whether it is caused by the same trapping mechanism as described in Ref. [23] or not.

That the measurements in Figures 38a and 38b both, albeit to a varying degree, exhibit a hysteresis in ΔG could explain why the OBIC scan shows "smearing" along the principal scanning direction (x-axis).

These results suggest that it is possible to use the open-circuit voltage of a single InP *n-i-p* NW to affect the current throughput of an InAs NW, *via* a field-effect gate. The OBIC scan and the power dependent measurements taken together, indicate that while there is an NPC effect originating from the InAs NW, it is distinct from the "photo-gating" effect caused by the InP NW.

4.2.3 PT8: device D1 (n-gate 2xInP/InAs)

In this Section, the device PT8-D1 (Figure 39a) is studied. PT8-D1 features two InP NWs connected in series, with the n-terminal of the final InP NW connected to the InAs gate. As such, the same qualitative gating effect as in the two previous devices is expected from this device; the main motivation is now to explore whether both InP NWs will contribute to gating the InAs NW. If so, simultaneous illumination of both InP NWs should effectively double the gating voltage acting on the InAs NW.

Figure 39b shows an OBIC scan of the device, performed using $P_{LD} = 49$ nW, $V_{SD} = 8$ mV and V_G=0 V, together with a to-scale overlay of the SEM image. The OBIC scan reveals two current minima, one broader, and one more focused and slightly offset to the right with regards to the broader minimum. As the overlay shows, both the separation between the current minima and their relative position agree approximately with the SEM image overview of the different parts of the device. At this voltage and illumination intensity, a reduction of current of about 4 nA (∼14%) is achieved when illuminating the InP NWs.

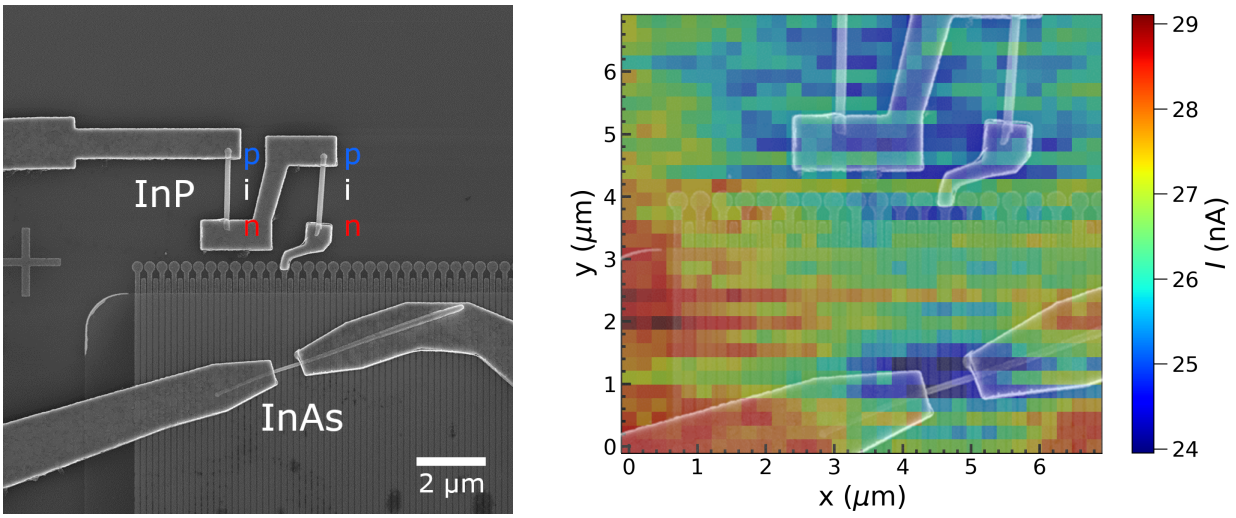

(a) **(b)**

Figure 39: (a) SEM image depicting the device PT8-D1: two InP NWs are connected in series with their n-terminals connected to the InAs gate. (b) OBIC scan of the same device, together with a to-scale overlay of the SEM image.

The OBIC scan presented in Figure 39b could suggest that both InP NWs of the device contribute to the gating of the InAs NW, but since it was not possible to resolve the two separate InP NWs, this is not certain. However, compared to the scan in Figure 37, the resolution of the current scan is improved, with both the InP and InAs current minima being more well-defined. This is most likely due to a more successful focusing of the LD beam in the case of the PT8-D1 scan.

As is evidenced by the much lower current at a higher V_{SD} bias, the resistance of the PT8-D1 InAs NW is markedly larger than that of the PT7-3 InAs NW. Since we are here dealing with individual single NWs, such variations are to be expected. Differences in resistance can be related to variations in e.g. NW crystal structure, NW thickness, and the quality of NW contacting by the Ti/Au leads.

4.2.4 PT8: device E1 (p-gate InP/InAs)

In this Section, the device PT8-E1 (depicted in Figure 40a) is investigated. The device consists of a single InP NW connected with the p-terminal to the InAs gate, i.e. the opposite configuration compared the devices tested so far. Thus, the expectation should be that illumination of the InP NW will increase the conductance of the InAs NW. In other words, the PT8-E1 device is designed to be able to perform the role of the excitatory subcomponent of the neuromorphic NW circuit in Ref. [13]. In addition to an OBIC scan, direct biasing of the InP NW by applying an external voltage V_G was tested for this device. This provides a possibility of comparing the gating effect of the applied voltage with the gating achieved by illumination of the InP NW.

As the OBIC scan (Figure 40b) shows, illumination of the InP NW increases the InAs current. Moving away from the InP NW, the current decreases, but for this device, no InAs NPC effect was detected.

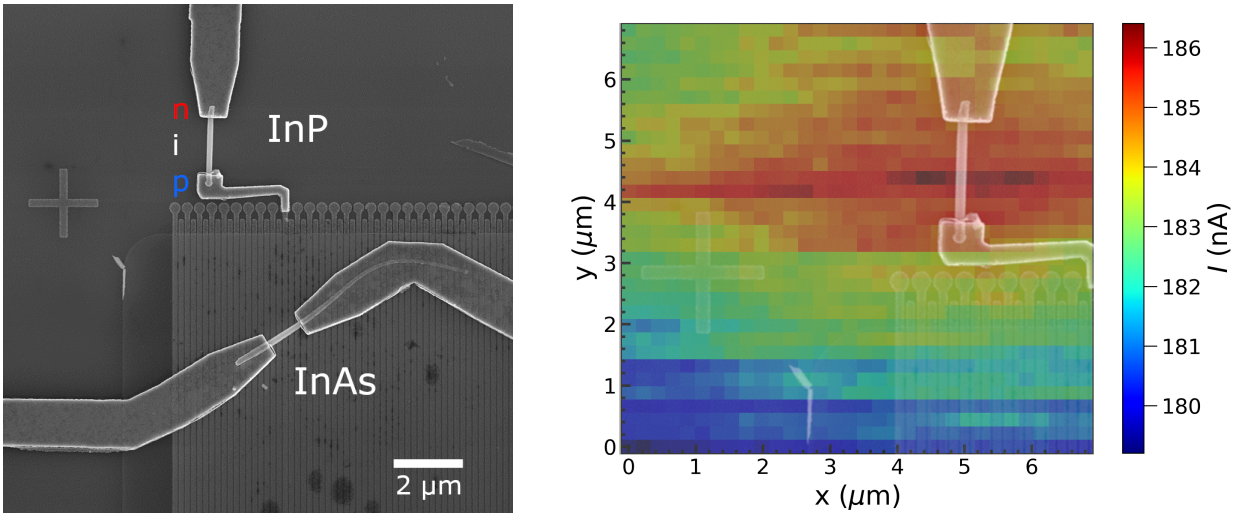

(a) **(b)**

Figure 40: a) SEM image depicting the device PT8-E1: a single InP NW is connected with the p-terminal to the InAs gate. (b) OBIC scan of the same device, together with a to-scale overlay of the SEM image.

Figure 41 shows how the InAs conductance changes as different voltages V_G are applied across the InP NW, with all illumination turned off. V_G was first set to 3 V and then stepped to -3 V in steps of 1 V (blue). V_G was then stepped back up from -3 V to +3 V (red). The last data point on the red curve was recorded after waiting ~ 30 s.

The OBIC scan indicates that the InP NW has the expected gating effect, and the effect of V_G on the InAs conductance strengthens the claim that the photo-gating is indeed caused by the open-circuit voltage of the InP NW. Based on the blue curve in Figure 41, the increase in InAs conductance relative to $V_G = 0$ V seems to saturate at ~ 15 μS. However, as indicated by the two final data points at +3 V (red curve), there is some time dependence in the gating effect, meaning that only tentative conclusions should be drawn from this data. Still, a power dependent measurement on the device yielded a similar maximal ΔG (Appendix G).

The lack of noticeable NPC in this device, could owe to individual variations among the different InAs NWs. Circumstantially, one can note that the exposed part of the InAs

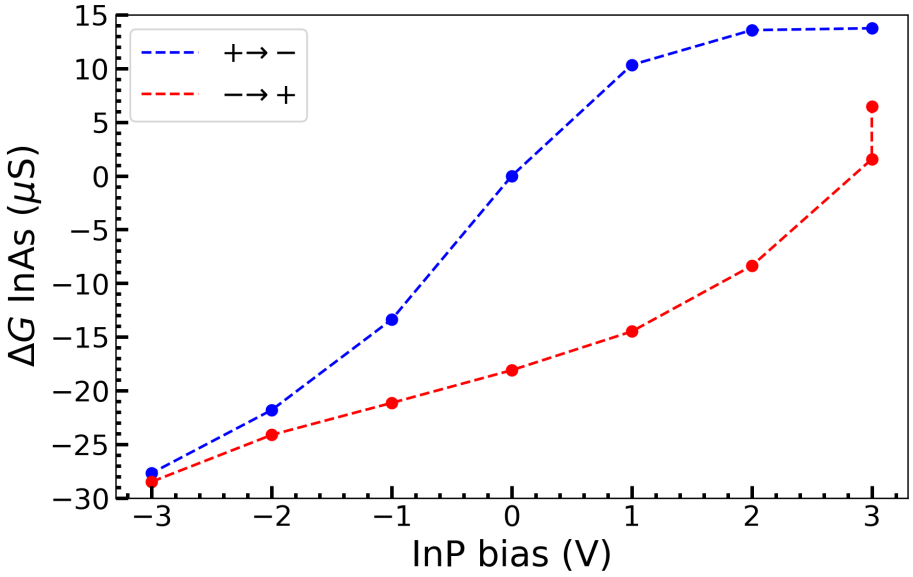

Figure 41: Study of device PT8-E1: InAs conductance as a function of InP bias (V_G). V_G was stepped from +3 V to -3 V (blue curve), and then up to +3 V again (red curve), in steps of 1 V. The last red curve data point at +3 V was recorded after waiting $\sim$ 30 s. Each data point is extracted from an InAs IV-sweep from -5 mV to +5 mV.

NW in PT8-E1 is close to the NW base, while the exposed part in PT7-3, PT7-9 and PT8-D1 lies close to the NW top (i.e. close to the Au-bead).

4.3 NW-to-NW Optical Communication

The results presented in this Section pertain to the subsystem highlighted in Figure 42, i.e. basic optical communication from one NW to another, without any intervening dye layer. Note that even though the device studied here is capable of NW-to-NW communication, the results presented here only relate to the optical emission of the NWs.

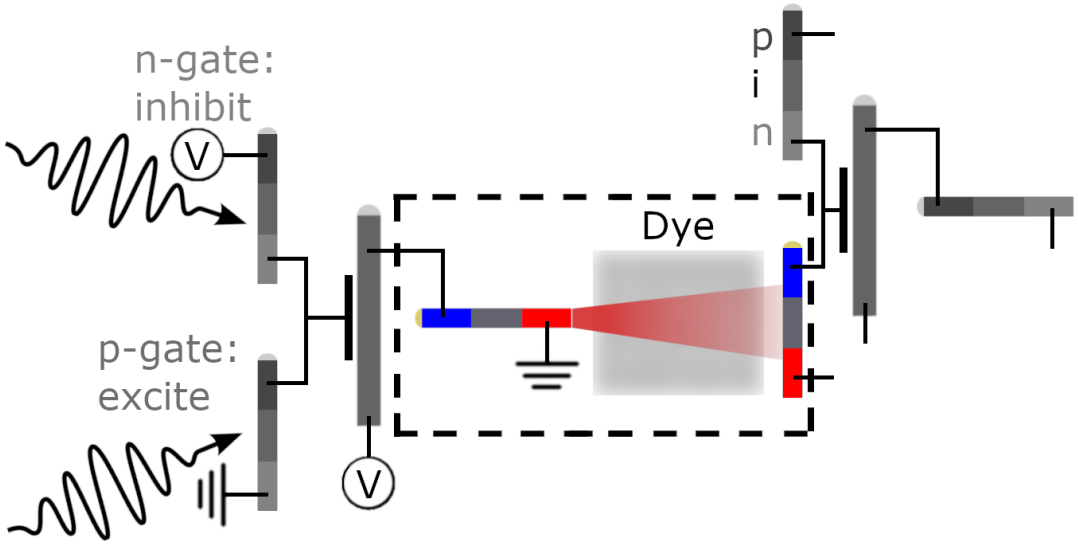

Figure 42: The highlighted part shows the subsystem which the results presented in this Section pertain to: the case of an InP NW emitting light towards another InP NW, without any intervening dye layer. Note that even though the device studied here is capable of NW-to-NW communication, the results presented here only relate to the optical emission of the NWs.

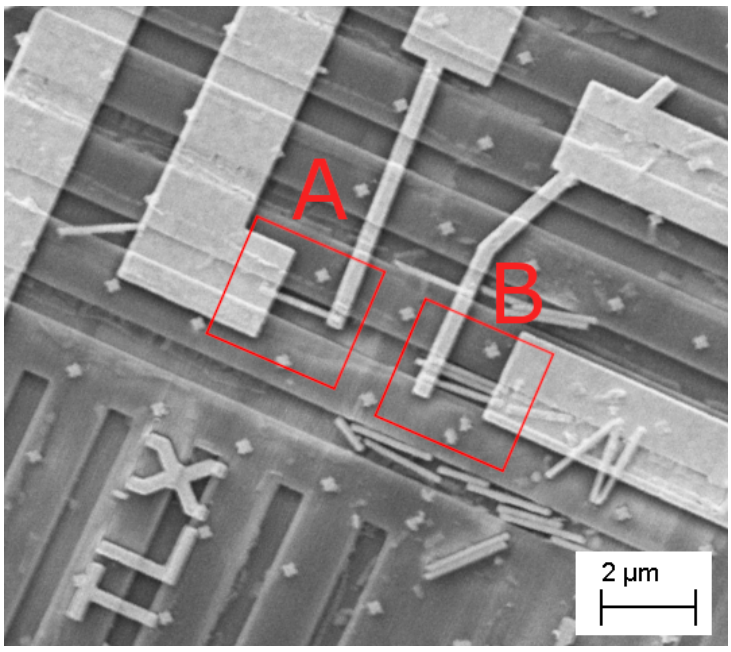

Figure 43: SEM image of the DFR1-FF TLX device.

The SEM image in Figure 43 depicts the device "TLX" on sample DFR1-FF, a sample in which trenches have been etched so as to facilitate the placement and alignment of InP

NWs. TLX consists of one NW contacted separately ("A" in Figure 43), and three NWs contacted together by the same leads ("B" in the Figure). Figure 44 shows TLX as imaged through the 100X objective lens while the sample is illuminated by the LED, with a false-color overlay in red which shows the recorded emission from the single NW in the device, at the same camera and sample position. The emission was captured as a movie while the NW bias was swept, with all light sources turned off. At sufficiently large currents, optical emission was detected, with the emission intensity co-varying with the current throughput. The overlay in red is a representative frame from the recorded movie. Figure 45 shows the same, but when instead the triple cluster is biased. The emission clearly overlaps with the NW(s) which are being biased. The detected optical emission can be seen as complementary to the OBIC scan of the InP *p-i-n* NW presented in Figure 33b.

These measurements provide confirmation that there is actual light emission at the relevant voltages used for the device communication experiment. The next step is to quantify the emission intensity, meaning that the CMOS camera would need to be calibrated against a well-known light source.

Appendix H shows the sample subarea which contains the TLX device area together with emission from the single NW, as imaged through the 20X objective of the setup.

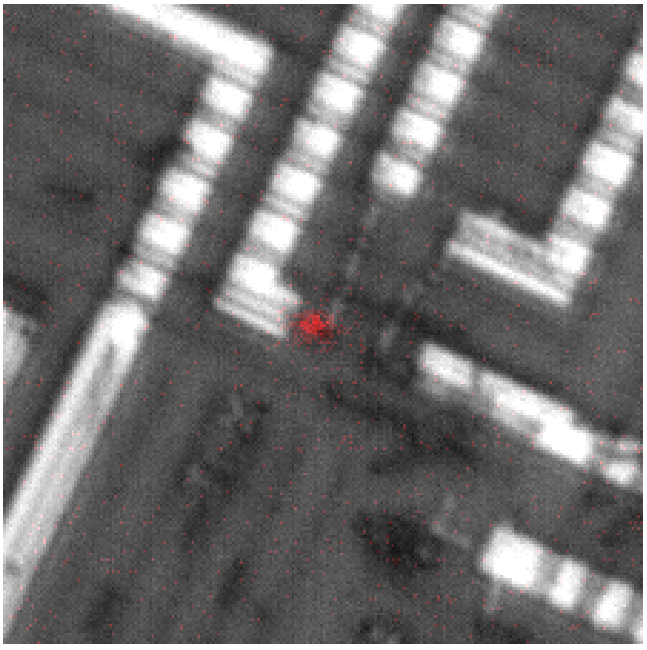

Figure 44: Light emission from a single InP NW detected by optical microscopy.

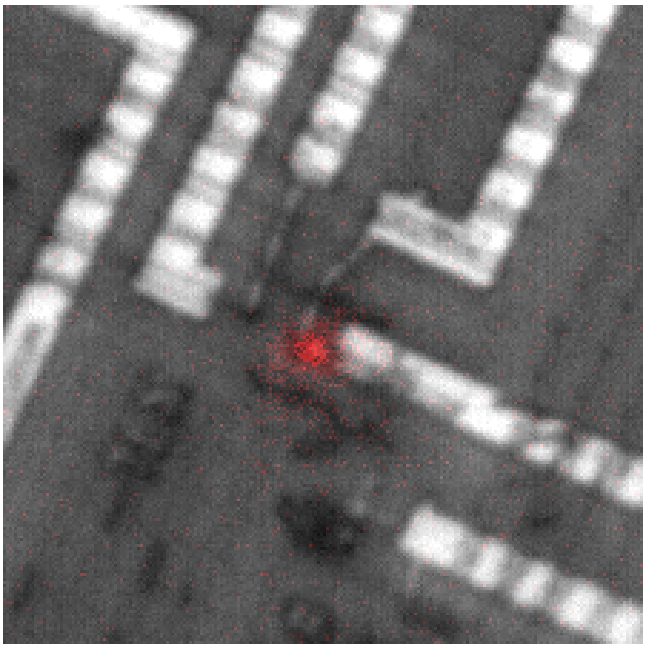

Figure 45: Light emission from a cluster of three InP NWs detected by optical microscopy.

5 Conclusion & Outlook

5.1 Molecular Memory Systems

We have shown that the DASA photoswitch D1A3/AP-048 suspended in a PAMS polymer film on top of a NW solar cell device confers a memory effect to the current response of the device under illumination conditions coinciding with the

A significant change in transmittance was achieved using a 5 mM dye solution with a 1%-wt dye-to-polymer ratio, deposited to yield a few μm thin film. The dye retained its photoswitching behavior independently of whether it was deposited on sapphire or a NWA solar cell device. The relation between illumination intensity and bleaching rate was investigated, as was the stability of the color recovery rate over time.

By using different illumination conditions, a high degree of repeatability of bleaching and recovery, using both constant and pulsed illumination was demonstrated.

A variety of characteristic time constants for both color bleaching and recovery have been demonstrated. It was found that drop cast films featured faster bleaching and recovery dynamics than spin coated films. Notably, the characteristic recovery time constants k of the drop cast films were similar to what was measured in solution, while the spin coated films featured recovery time constants 2 orders of magnitude smaller. Upon annealing at 70°C, the different film types converged to values of k close to the original spin coated film k. These differences likely reflect that the polymer structure in drop cast films is more similar to that in solution; annealing induces changes of the polymer matrix, leading to a structure similar to what is achieved by spin coating. These effects should be investigated more closely by comparing a larger sample set of spin coated and drop cast samples, before and after annealing at different temperatures and times.

5.2 NW Opto-Electronics

The results presented in this Section, suggest that the principal design of the tested n- and p-gated NW opto-electronics devices is sound. In other words, the results show that it is possible both to engineer a functioning single NW field effect gate, and to use the photoresponse of another NW to generate the gate bias V_G.

Based on these encouraging results, devices which feature both an n-gating and a p-gating InP NW connected to the same InAs NW were constructed, in order to more fully realize parts of the hypothetical NW circuit depicted in Figure 3. Early results (Figure 46b) indicate that this device has the desired functionality The combination of exciting and inhibiting optical signaling capabilities is an essential part of a computationally relevant neural node NW circuit explored using simulations in Refs. [9] [13]. The role of the charge-based memory included in the circuit in Ref. [13] could possibly be filled by the observed time-dependent gate hysteresis (Figure 41).

The resistance of the PT8-D1 InAs NW is markedly larger than the PT7-3 InAs NW. This highlights a possible challenge in future device production, as a highly consistent NW resistance is a prerequisite for neural network scalability using these devices. This challenge relates both to the NW growth, and the assembling and contacting of single NWs. Scalable and accurate alignment and placement of NWs could be achieved by e.g. Molecular Beam Epitaxy [32][33], possibly in conjunction with dielectrophoresis [34].

In the immediate future, further characterization of the class of doubly gated devices depicted in Figure 46a will follow. For future studies it would additionally be highly

desirable to more diligently explore the hysteresis and its time-dependence for the various NW electronics devices. Such studies are motivated not only by that these effects affect device performance, but also since such effects could be utilized as an integrated neural node memory, akin to the functionality provided by the molecular dye also investigated in this work.

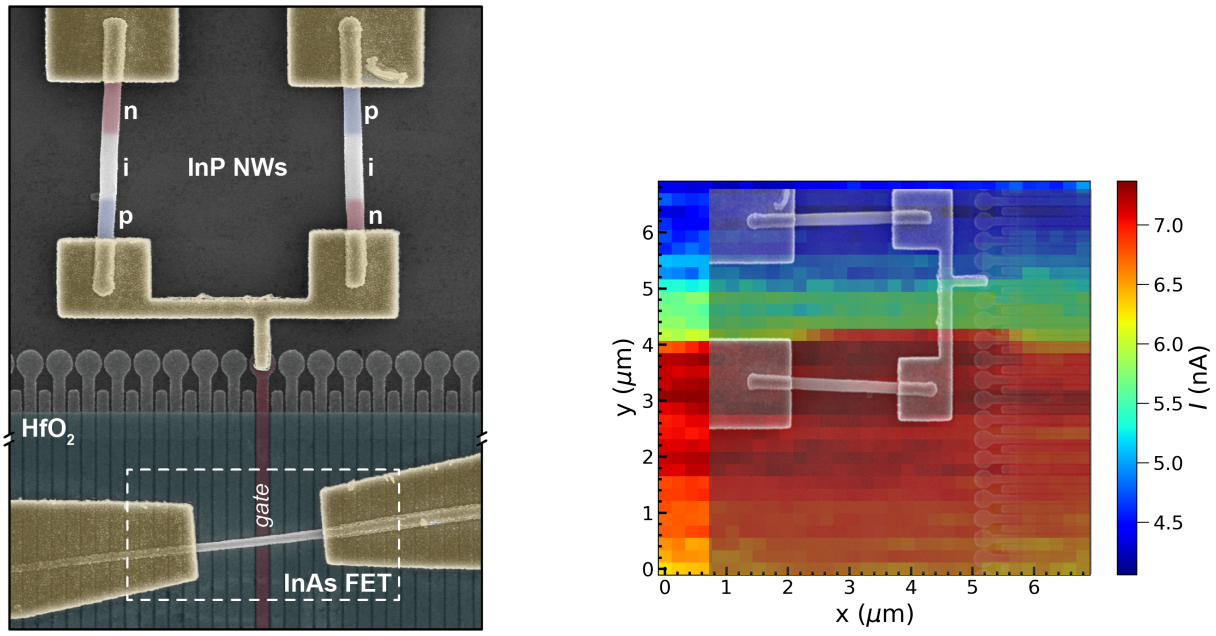

(a) (b)

Figure 46: (a) False-color SEM image of the latest generation of InP-gated InAs FET devices. Note that the y-axis is cut. (b) OBIC scan of the InP-region of the device depicted in (a), with an overlay of the SEM image. Note that the excitatory and inhibitory regions of the OBIC scan agree with both InP NW separation and orientation.

5.3 NW-to-NW Optical Communication

The results presented in the Section provide confirmation that optical emission from single p-i-n doped InP NWs, of the same type as are used in the opto-electronic devices studied in this work, does occur. This result corroborates and strengthens the claim that the NW-to-NW communication observed in an independent study using the specific device pair tested here, indeed was optically mediated.

The emission wavelength of intrinsic InP is centered on $\lambda_g \simeq 923$ nm, i.e. some 300 nm longer than the absorption maximum of the DASA dye investigated here. This means that realization of the circuit in Figure 3 requires the alteration of either or both of these characteristics. Research towards DASA photoswitches which absorb at longer wavelengths is ongoing but likely complex, as the spectral and relevant temporal characteristics of the dye molecules are interdependent. Instead, $Ga_xIn_{1-x}P$ NWs could be used in place of the InP NWs, since the fractional gallium content can be tailored to provide band gap energies up to ~ 2 eV.

5.4 Final Notes

The connecting of single NWs into functioning circuits is still a young field, but it is encouraging that the constructed devices so far seem to behave as one would expect, based on the properties of the individual NWs.

The results presented in this Thesis provide concrete and direct steps towards achieving several of the milestones along the path towards the neuoromorphic device which is the long-term goal of the Horizon Europe InsectNeuroNano research project. By combining the various subsystems studied here: a polymer layer containing the reversibly bleachable DASA photoswitch, and optically activated NW FET devices applied to control the driving current through light-emitting NWs, a fairly complex device capable of providing a versatile functionality as nodes in a neuromorphic network, could be achieved.

References

[1] D. Marković, A. Mizrahi, D. Querlioz, and J. Grollier, "Physics for neuromorphic computing," *Nature Reviews Physics*, vol. 2, no. 9, pp. 499–510, 2020.

[2] X. Xu, Y. Ding, S. X. Hu, M. Niemier, J. Cong, Y. Hu, and Y. Shi, "Scaling for edge inference of deep neural networks," *Nature Electronics*, vol. 1, pp. 216–222, 2018.

[3] P. R. Prucnal and B. J. Shastri, *Neuromorphic photonics*. CRC press, 2017.

[4] V. K. Sangwan and M. C. Hersam, "Neuromorphic nanoelectronic materials," *Nature nanotechnology*, vol. 15, no. 7, pp. 517–528, 2020.

[5] S. Woźniak, A. Pantazi, T. Bohnstingl, and E. Eleftheriou, "Deep learning incorporating biologically inspired neural dynamics and in-memory computing," *Nature Machine Intelligence*, vol. 2, no. 6, pp. 325–336, 2020.

[6] "Nvidia jetson tx2 specifications." `https://developer.nvidia.com/embedded/jetson-tx2`. Accessed: 2023-11-23.

[7] I. Pisokas, S. Heinze, and B. Webb, "The head direction circuit of two insect species," *eLife*, vol. 9, 2020.

[8] R. N. Patel, J. Kempenaers, and S. Heinze, "Vector navigation in walking bumblebees," *Current Biology*, vol. 32, pp. 2871–2883, 2022.

[9] D. O. Winge, S. Limpert, H. Linke, M. T. Borgström, B. Webb, S. Heinze, and A. Mikkelsen, "Implementing an insect brain computational circuit using iii-v nanowire components in a single shared waveguide optical network," *ACS Photonics*, vol. 10, pp. 2787–2798, 2020.

[10] D. Alcer, L. Hrachowine, D. Hessman, and M. T. Borgström, "Processing and characterization of large area inp nanowire photovoltaic devices," *Nanotechnology*, vol. 34, no. 29, p. 295402, 2023.

[11] C. Thelander, K. A. Dick, M. T. Borgström, L. E. Fröberg, P. Caroff, H. A. Nilsson, and L. Samuelson, "The electrical and structural properties of n-type inas nanowires grown from metal–organic precursors," *Nanotechnology*, vol. 21, no. 20, p. 205703, 2010.

[12] P. Krogstrup, H. Jørgensen Ingerslev, M. Heiss, O. Demiche, V. J. Holm, M. Aagesen, J. Nygard, and A. Fontcuberta i Morral, "Single-nanowire solar cells beyond the shockley-queisser limit," *Nature Photonics*, vol. 7, 2013.

[13] D. Winge, M. Borgström, E. Lind, and A. Mikkelsen, "Artificial nanophotonic neuron with internal memory for biologically inspired and reservoir network computing," *Neuromorph. Comput. Eng.*, vol. 3, no. 034011, 2023.

[14] B. J. Shastri, A. N. Tait, T. Ferreira de Lima, W. H. Pernice, H. Bhaskaran, C. D. Wright, and P. R. Prucnal, "Photonics for artificial intelligence and neuromorphic computing," *Nature Photonics*, vol. 15, no. 2, pp. 102–114, 2021.

[15] Y. Bai, X. Xu, M. Tan, Y. Sun, Y. Li, J. Wu, R. Morandotti, A. Mitchell, K. Xu, and D. J. Moss, "Photonic multiplexing techniques for neuromorphic computing," *Nanophotonics*, vol. 12, no. 5, pp. 795–817, 2023.

[16] Y. Shen, N. C. Harris, S. Skirlo, M. Prabhu, T. Baehr-Jones, M. Hochberg, X. Sun, S. Zhao, H. Larochelle, D. Englund, *et al.*, "Deep learning with coherent nanophotonic circuits," *Nature photonics*, vol. 11, no. 7, pp. 441–446, 2017.

[17] T. Zhou, X. Lin, J. Wu, Y. Chen, H. Xie, Y. Li, J. Fan, H. Wu, L. Fang, and Q. Dai, "Large-scale neuromorphic optoelectronic computing with a reconfigurable diffractive processing unit," *Nature Photonics*, vol. 15, no. 5, pp. 367–373, 2021.

[18] N. H. Farhat, D. Psaltis, A. Prata, and E. Paek, "Optical implementation of the hopfield model," *Appl. Opt.*, vol. 24, pp. 1469–1475, May 1985.

[19] G. Otnes, E. Barrigón, C. Sundvall, K. E. Svensson, M. Heurlin, G. Siefer, L. Samuelson, I. Åberg, and M. T. Borgström, "Understanding inp nanowire array solar cell performance by nanoprobe-enabled single nanowire measurements," *Nano Letters*, vol. 18, no. 5, pp. 3038–3046, 2018. PMID: 29701974.

[20] J. Fast, Y.-P. Liu, Y. Chen, L. Samuelson, A. M. Burk, H. Linke, and A. Mikkelsen, "Optical-beam-induced current in inas/inp nanowires for hot-carrier photovoltaics," *ACS Appl. Energy Mater.*, vol. 5, no. 6, pp. 7728–7734, 2022.

[21] S. M. Sze and M.-K. Lee, *Semiconductor Devices: Physics and Technology*. Wiley, 3 ed., 2012.

[22] K. Y. Cheng, *III–V Compound Semiconductors and Devices*. Springer, 2020.

[23] Y. Yang, X. Peng, H.-S. Kim, T. Kim, S. Jeon, H. K. Kang, W. Choi, J. Song, Y.-J. Doh, and D. Yu, "Hot carrier trapping induced negative photoconductance in inas nanowires toward novel nonvolatile memory," *ACS NanoLetters*, vol. 15, pp. 5875–5882, 2015.

[24] C. F. Bohren and D. R. Huffman, *Absorption and Scattering of Light by Small Particles*. Wiley, 1998.

[25] B. Valeur and M. N. Berberan-Santos, *Molecular Fluorescence: Principles and Applications*. Wiley-VCH, 2 ed., 2012.

[26] S. Helmy, S. Oh, F. A. Leibfarth, C. J. Hawker, and J. R. de Alaniz, "Design and synthesis of donor-acceptor stenhouse adducts: A visible light photoswitch derived from furfural," *J. Org. Chem.*, vol. 79, pp. 11316–11329, 2014.

[27] N. Ceberg and J. S. Nilsson, *Modelling photoswitching dye memory for path integration*. M.Sc. Thesis. Department of Computer Science, LTH, Lund University, 2022.

[28] T. W. Hughes, M. Minkov, Y. Shi, and S. Fan, "Training of photonic neural networks through in situ backpropagation and gradient measurement," *Optica*, vol. 5, no. 7, pp. 864–871, 2018.

[29] E. Hairer, S. P. Norsett, and G. Wanner, *Solving Ordinary Differential Equations I: Nonstiff Problems*. Springer, 1993.

[30] Y.-P. Liu, *Surface and interfaces of low dimensional III-V semiconductor devices*. Division of Synchrotron Radiation, Department of Physics, Lund University, 2022.

[31] J. Heo, D. P. Murale, H. Y. Yoon, V. Arun, S. Choi, E. Kim, J.-S. Lee, and S. Kim, "Recent trends in molecular aggregates: An exploration of biomedicine," *Aggregate*, vol. 3, no. 2, p. e159, 2022.

[32] P. Aseev, A. Fursina, F. Boekhout, F. Krizek, J. E. Sestoft, F. Borsoi, S. Heedt, G. Wang, L. Binci, S. Martí-Sánchez, T. Swoboda, R. Koops, E. Uccelli, J. Arbiol, P. Krogstrup, L. P. Kouwenhoven, and P. Caroff, "Selectivity map for molecular beam epitaxy of advanced iii–v quantum nanowire networks," *Nano Letters*, vol. 19, no. 1, pp. 218–227, 2019.

[33] S. Vaitiekėnas, A. Whiticar, M.-T. Deng, F. Krizek, J. Sestoft, C. Palmstrøm, S. Marti-Sanchez, J. Arbiol, P. Krogstrup, L. Casparis, and C. Marcus, "Selective-area-grown semiconductor-superconductor hybrids: A basis for topological networks," *Physical Review Letters*, vol. 121, no. 14, 2018.

[34] S. K. Jangir, H. K. Malik, P. Saho, R. Muralidharan, T. Srinivasan, and P. Mishra, "Electrical transport and gas sensing characteristics of dielectrophoretically aligned mbe grown catalyst free inas nanowires," *Nanotechnology*, vol. 30, no. 10, 2019.

A Thickness measurements of some dye/polymer films

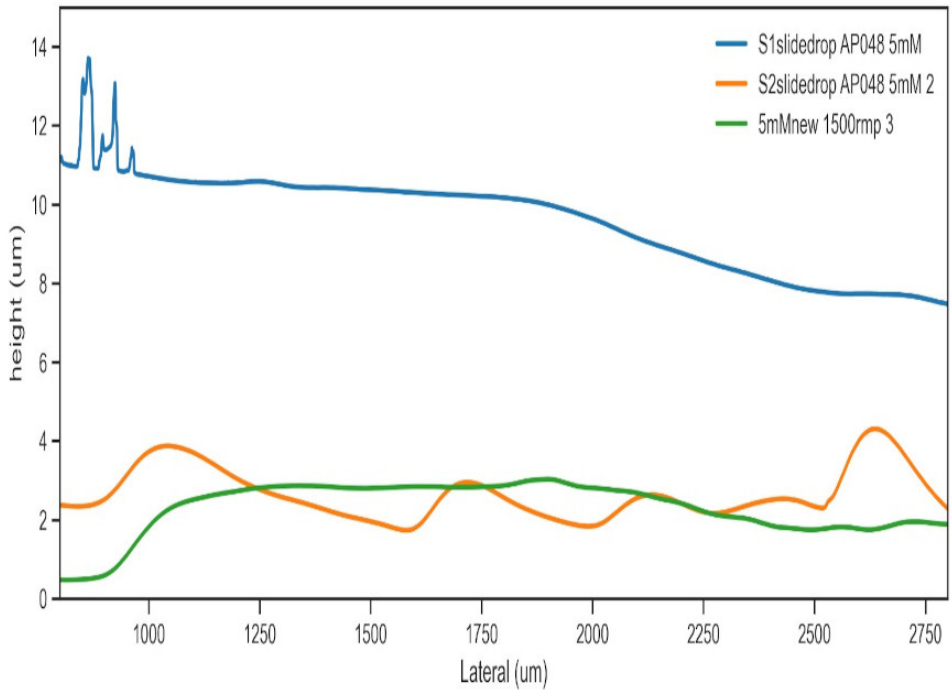

Figure 47: Measurement results from the profilometer line scans on dye-on-sapphire samples: the film thickness of two drop cast samples (blue and orange), and one spin coated at 1500 rpm (green). Height in μm as a function of lateral distance in μm. Note that the spin coated sample has a more uniform film thickness than the two drop cast samples.

B Dye+NWA experimental parameters

The illumination source was the 633-711 nm LED of the G2V Pico Solar Simulator.

Table 4

(a) Parameters for the "Pyramids" measurement. The t_{off} between sets 7 and 8 is 24000 s (about 6 h 40 min).

Set #	t_{off} (s)	t_{low}	t_{high}	I_{low}	I_{high}	Repetitions
1 & 8	2400	2000	1000	35	150	6
2 & 9	2400	2000	1000	35	350	6
3 & 10	2400	2000	1000	35	550	6
4 & 11	2400	2000	1000	35	1000	6
5 & 12	2400	2000	1000	35	550	6
6 & 13	2400	2000	1000	35	350	6
7 & 14	2400	2000	1000	35	150	6

(b) Parameters for the "Pulses" measurement.

Set #	t_{off} (s)	t_{low}	t_{high}	I_{low}	I_{high}	Repetitions
1	1000	5	5	35	150	20
2	1000	10	5	35	150	20
3	1000	20	5	35	150	20
4	1000	5	10	35	150	20
5	1000	10	10	35	150	20
6	1000	20	10	35	150	20
7	1000	40	5	35	150	20
8	1000	5	2.5	35	150	20
9	1000	10	2.5	35	150	20
10-14	1000	5	5	35	150	20

Table 5: Conversion table between the intensity values used by the Solar Simulator software and total irradiance in mW/cm^2 for the LED used, as provided by the software.

Solar Simulator	mW/cm^2
35	0.1
150	0.4
350	0.9
550	1.3
1000	2.4

C ΔI_{max} explained

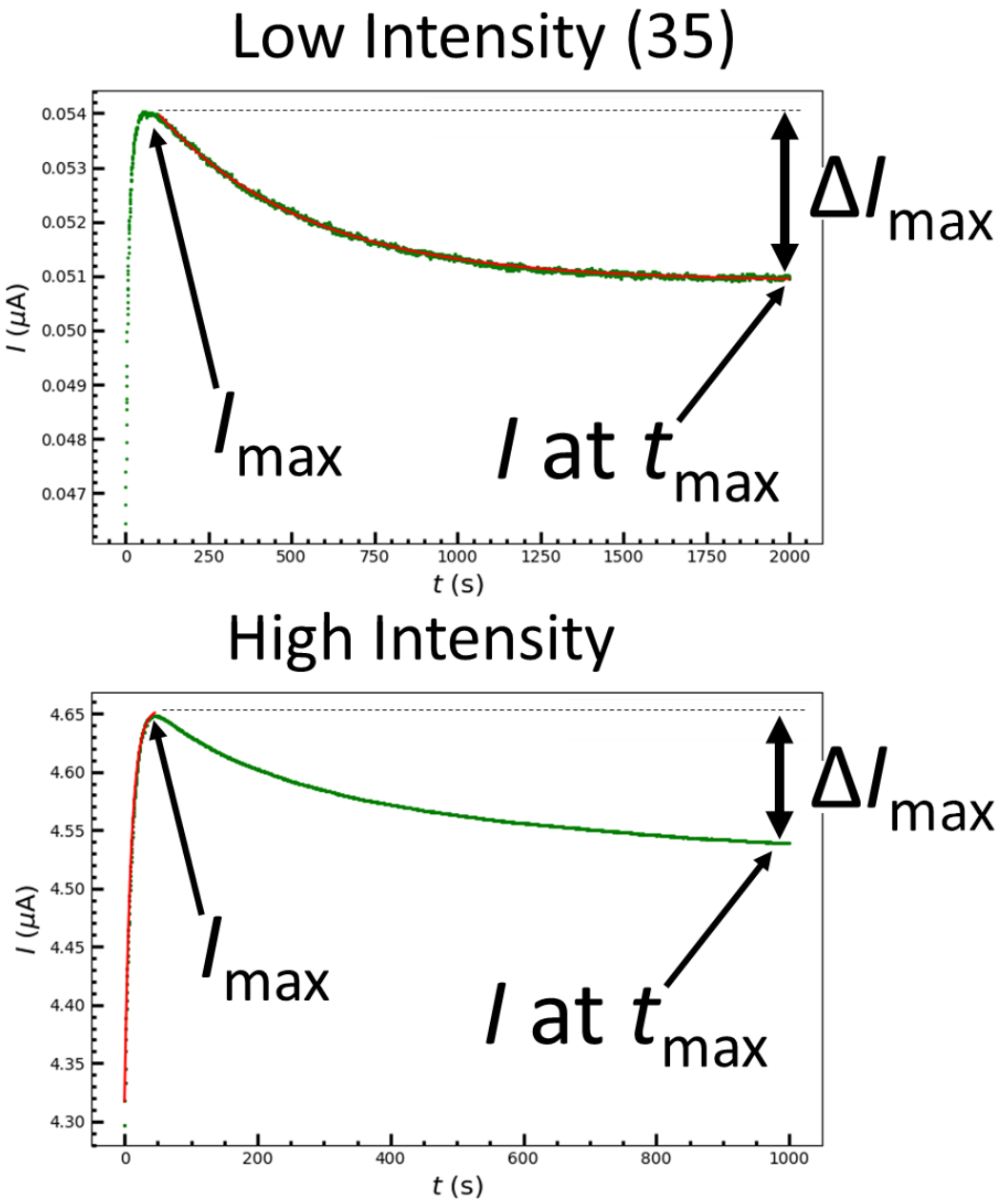

Figure 48: Definition of the ΔI_{max} property, pertaining to the "Pyramids" data set in section 4.1. The upper Figure is representative for the low intensity (*read*) periods, while the lower Figure is representative for the high intensity (*write*) periods of the "Pyramids" data set. The red line is an exponential fit, and marks the sections which are of interest for the two above curves respectively, and for which the time constants k have been plotted in Figure 28.

D Characterization of G2V Pico LED

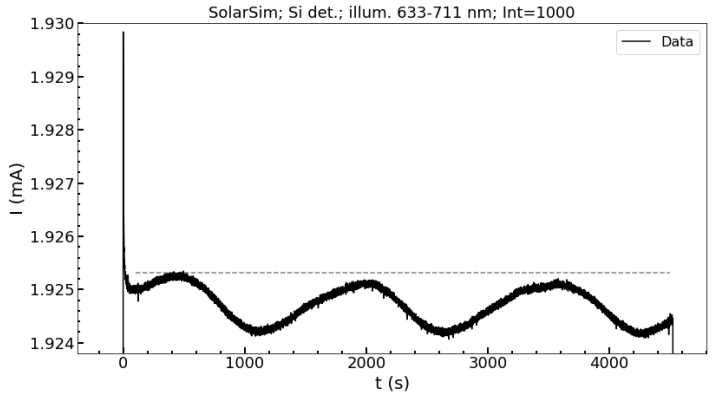

(a)

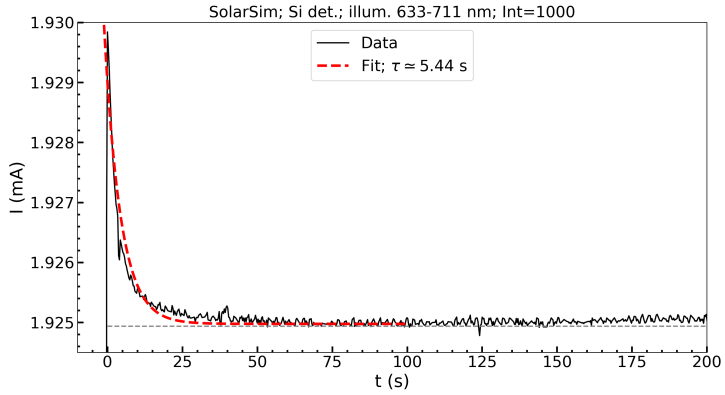

(b)

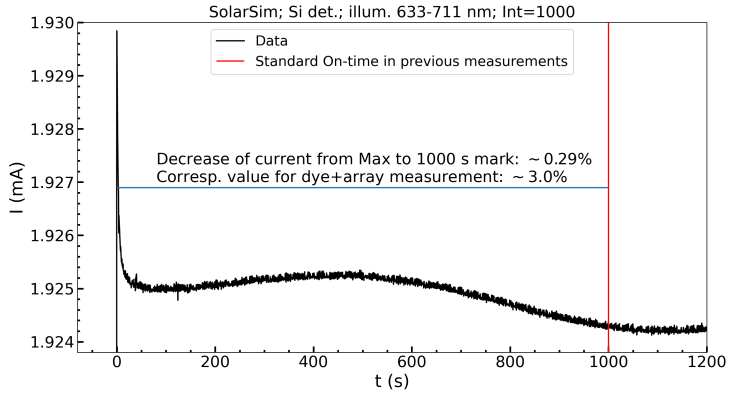

(c)

Figure 49: A Si photodiode was used to investigate the stability of the G2V Pico Solar Simulator 633-711 nm LED over time, at intensity 1000. (a) Full measurement. (b) First 200 seconds of the measurement, with an exponential fit. (c) First 1200 seconds of the measurement. The lamp intensity varies somewhat over time, but at much smaller relative magnitude than the measured change in Figure 25 on the relevant time scale.

E NW Electronics Experimental Parameters

Table 6: Experimental parameters relevant to the OBIC scans presented here.

	PT7-12	**PT7-3**	**PT8-D1**	**PT8-E1**
P_{LD} (W)	11E-9	11E-9	49E-9	49E-9
V_{sd} (mV)	0	2	8	0
V_g (V)	-	0	0	0
Scan window (μm)	5×5	6.8×6.8	6.8×6.8	6.8×6.8
Scan speed (nm/s)	200	500	500	500
Pixel size	48×48	32×32	32×32	32×32

F Device PT7-9

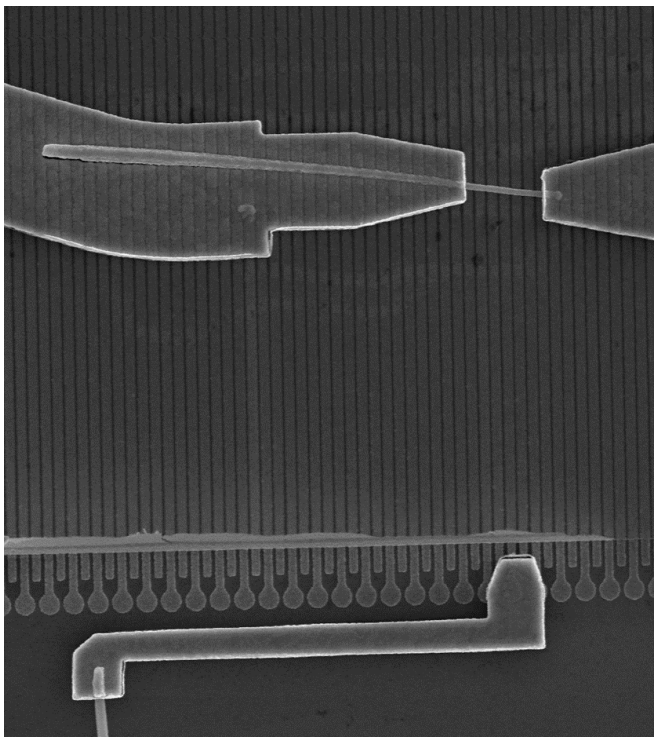

Figure 50: SEM image of Device 9 on sample PT7.

G Device PT8-E1

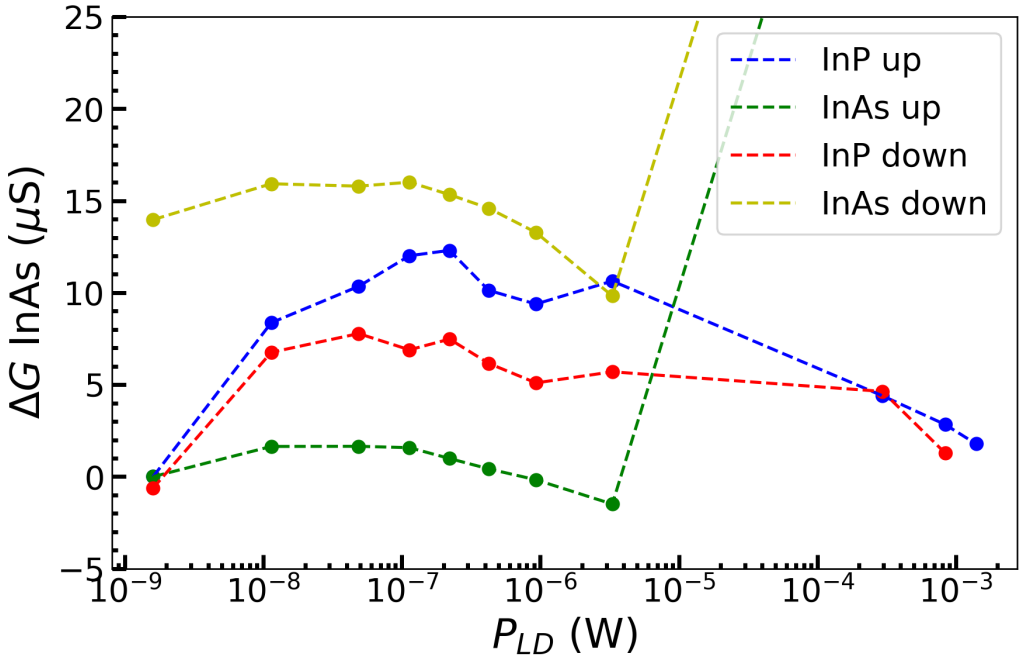

Figure 51: Power dependent measurement on device PT8-E1.

H Device DFR1-FF TLX

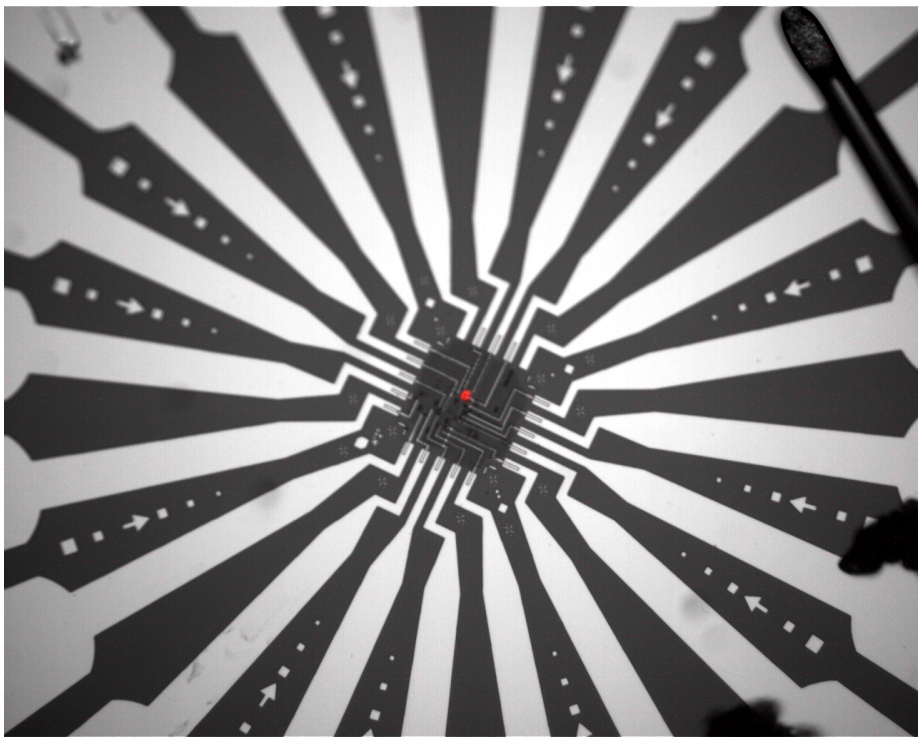

Figure 52: The area of sample DFR1-FF that contains the TLX device, as imaged through the 20X objective lens. The anchoring point of one of the wirebonds contacting the device is visible in the top right corner of the image. The false-color overlay in red shows the light emission by the single NW in the TLX device, as registered by the CMOS camera through the 20X objective.